

Topological classification of Higher-order topological phases with nested band inversion surfaces

Zhoutao Lei,¹ Yuangang Deng,^{1,*} and Linhu Li^{1,†}

¹*Guangdong Provincial Key Laboratory of Quantum Metrology and Sensing & School of Physics and Astronomy, Sun Yat-Sen University (Zhuhai Campus), Zhuhai 519082, China*

(Dated: June 24, 2022)

Higher-order topological phases (HOTPs) hold gapped bulk bands and topological boundary states localized in boundaries with codimension higher than one. In this work, we provide a unified construction and topological characterization of HOTPs for the full Altland-Zirnbauer tenfold symmetry classes, based on a method known as the nested band inversion surfaces (BISs). Specifically, HOTPs built on this method are decomposed into a series of subsystems, and higher-order topological boundary states emerges from the interplay of their 1st-order topology. Our analysis begins with a general discussion of HOTPs in continuous Hamiltonians for each symmetry class, then moves on to several lattice examples illustrating the topological characterization based on the nested-BIS method. Despite that the example minimal models possess several spatial symmetries, our method does not rely on any spatial symmetry, and can be easily extended into arbitrary orders of topology in dimensions. Furthermore, we extend our discussion to systems with asymmetric boundary states induced by two different mechanisms, namely crossed BISs that break a C_4 rotation symmetry, and non-Clifford operators that break certain chiral-mirror symmetries of the minimal models.

I. INTRODUCTION

Topological quantum matters, which are characterized by topological indices and host in-gap boundary states, have attracted much attention over the past decade [1, 2]. In the last few years, higher-order topological phases (HOTPs) beyond the conventional bulk-boundary correspondence principle have been introduced, i.e. a d -dimensional (d D) n th-order topological phase supports topologically protected boundary states in their $(d-n)$ D boundaries [3–6]. In contrast to conventional (1st-order) boundary states that have one dimension lower than the bulk, emergence of higher-order boundary states (e.g. corner states in 2D or higher) may depend not only on the bulk band topology, but also on properties of the system's boundaries. Accordingly, HOTPs have been classified into two categories: (i) “intrinsic” HOTPs associated with spatial-symmetry-protected bulk topology, and (ii) “extrinsic” HOTPs, whose topological properties rely on boundary termination of the system and require no protection from any spatial symmetry [7, 8]. In particular, a concept closely related to the latter is the boundary-obstructed HOTPs, which host robust higher-order boundary states in association with bulk quantities, even their emergence and disappearance do not involve bulk gap-closing under the periodic boundary condition (PBC) [9–13].

Owing to the rich and sophisticated topological origins rooted in the bulk and/or boundary of the systems, constructing and topologically characterizing HOTPs has been of great interest since their discovery [3–34]. Recently, novel boundary-obstructed HOTPs with nontrivial bulk topological invariants have been unveiled for the

A (without chiral symmetry) and AIII (with chiral symmetry) classes [33, 34] of the Altland-Zirnbauer (AZ) tenfold classes [35–38], broadening the scope of topological matters for these two complex symmetry classes. On the other hand, the complete classification involves another two non-spatial symmetries, namely the time-reversal symmetry \mathcal{T} and particle-hole symmetry \mathcal{C} . These two anti-unitary symmetries not only give rise to the eight real symmetry classes of the AZ classification, but are also tightly related to some intriguing properties of the systems. For instance, a time-reversal symmetric system with half-integer spin ensures Kramers degeneracy of its eigenvalues, and particle-hole symmetry naturally arise in the Bogoliubov-de Gennes Hamiltonian describing superconductors and superfluids, which allows for the possibility of inducing zero-energy Majorana modes [39, 40]. Nonetheless, a universal method for constructing and characterizing boundary-obstructed HOTPs with nontrivial bulk topological invariants for the full AZ classes is still absent in contemporary literature.

The starting point of this work is a method known as the nested band inversion surfaces (BISs), which has been employed to explore HOTPs in A and AIII classes of the AZ classes [34]. This method is built on the concept of BISs, which offers a powerful and innovative approach to probe 1st-order topological invariants through quantum dynamics [41–43]. Inhabiting this advantage, the nested-BIS method allows us to construct higher-order topology from 1st-order one of different parts of the system's Hamiltonian. To give an overview of HOTPs for the full AZ classes in arbitrary dimensions, we start from a systematic analysis of minimal continuous models supporting HOTPs in each symmetry class. The characterization of these HOTPs based on the nested-BIS method is then given by considering several 2D and 3D lattice examples converted from the continuous models. Specifically, n th-order topological phases with Z -type topology

* dengyg3@mail.sysu.edu.cn

† lilh56@mail.sysu.edu.cn

can be categorized as Z^n and $2Z^n$ classes, both characterized by n -fold Z topological invariants, while the number of higher-order boundary states will be double for the latter one. On the other hand, HOTPs with Z_2 topology are characterized by a Z_2 invariant and a set of Z invariants, denoted as $Z_2 \times Z^{n-1}$ classes accordingly. These topological indexes are shifted between different rows or columns in the symmetry classification table for different n (orders of topology), meaning that many HOTPs would be identified as trivial phases, or phases with different types of topology, in the conventional (1st-order) topological band theory. Finally, we extend our discussion to two scenarios beyond the standard nested-BIS method. Namely, asymmetric parameters along different directions may lead to crossed BISs, and a nested relation can only be recovered by taking into account high-order BISs [42]. Secondly, the standard nested-BIS method requires the Hamiltonian to be formed by Clifford operators [34], and a generalization of this method for systems with certain non-Clifford operators is established with extra effective surface BISs. Interestingly, in both cases, certain spatial symmetries are broken by the extra modulations, resulting in asymmetric properties of higher-order boundary states in our systems.

The rest of this paper is organized as follows. In Sec II, we review the nested-BIS method and establish a general Hamiltonian for HOTPs. Sec III present the symmetry classification and the continuous Hamiltonians of HOTPs characterized by integer topological invariant. The corresponding minimal lattice Hamiltonian for several examples are provided in Sec IV. Next we derive HOTPs with Z_2 topological invariant in Sec V, which complete the five topologically nontrivial classes in every spatial dimension of the AZ classification table. In Sec VI, we explore asymmetric properties of HOTPs, and extend the nested-BIS to Hamiltonians beyond the Clifford algebra. Lastly, a brief summary and discussion of our results are given in Sec VII.

II. THE NESTED BAND INVERSION SURFACES

We begin with an introduction of the nested-BIS method for constructing and characterizing HOTPs with arbitrary orders of topology in arbitrary dimensions [34]. This method is built on the BISs and high-order BISs used to dynamically characterize the first-order topological phases, where m th-order BISs are given by a special region in the Brillouin zone with m vanishing pseudo-spin components of the Hamiltonian, denoted as m -BISs [41, 42]. Following the nested-BIS method, a d D Hamiltonian hosting n th-order topology can be constructed as

$$H = \mathbf{h}(\mathbf{k}) \cdot \boldsymbol{\gamma} = \sum_j^J h_j(\mathbf{k}) \gamma_j, \quad (1)$$

where γ_j are the operators from the Clifford algebra satisfying $\{\gamma_i, \gamma_j\} = 2\delta_{i,j}$, $\mathbf{k} = (k_1, k_2, \dots, k_d)$ is the d D momentum, and $J = d + n$. We assume that k_i is only contained in $(h_1, h_2, \dots, h_{2i})$ for $\forall i < n$ (in principle, this condition can always be satisfied through some rotations and deformations for systems with only nearest neighbor hoppings), e.g. k_1 is contained only in h_1 and h_2 , and divide Hamiltonian of Eq. (1) into $n - 1$ two-component Hamiltonian terms and one $(d - n + 2)$ -component Hamiltonian term:

$$\begin{aligned} H_1(\mathbf{k}) &= h_1(\mathbf{k})\gamma_1 + h_2(\mathbf{k})\gamma_2, \\ H_2(\mathbf{k}_{1,\parallel}) &= h_3(\mathbf{k}_{1,\parallel})\gamma_3 + h_4(\mathbf{k}_{1,\parallel})\gamma_4, \\ &\dots \\ H_{n-1}(\mathbf{k}_{n-2,\parallel}) &= h_{2n-3}(\mathbf{k}_{n-2,\parallel})\gamma_{2n-3} \\ &\quad + h_{2n-2}(\mathbf{k}_{n-2,\parallel})\gamma_{2n-2}, \\ H_n(\mathbf{k}_{n-1,\parallel}) &= \sum_{j=2n-1}^J h_j(\mathbf{k}_{n-1,\parallel})\gamma_j, \end{aligned} \quad (2)$$

where $\mathbf{k}_{i,\parallel} = (k_{i+1}, k_{i+2}, \dots, k_d)$. With this construction, we can now define a BIS and a topological invariant for each H_i , and the overall n th-order topology can be characterized by the nested relation of these BISs and the collection of these topological invariants, as elaborated below.

For each two-component Hamiltonian H_i with $i < n$, a winding number v_i can be defined as a function of the $(d - i)$ D momentum $\mathbf{k}_{i,\parallel}$,

$$v_i(\mathbf{k}_{i,\parallel}) = \frac{1}{2\pi} \oint_{k_i} \frac{h_{2i-1}dh_{2i} - h_{2i}dh_{2i-1}}{h_{2i-1}^2 + h_{2i}^2}. \quad (3)$$

The $(d - i)$ D surface Brillouin zone (BZ) expanded by $\mathbf{k}_{i,\parallel}$ is then divided into distinct regimes with different values of v_i . The boundaries between these regimes are given by $h_{2i-1} = h_{2i} = 0$, which by definition are a second-order BIS (2-BIS) of the system [42], denoted as $S_i^{m=2}$ with m specifying the order of the BIS. Finally, another topological invariant v_n is defined for the $(d - n + 1)$ D Hamiltonian H_n and can be extracted from the pseudospin textures at its BIS S_n^m [41]. Note that in contrast to the rest 2-BIS $S_i^{m=2}$ with $i < n$, the order of S_n^m is not specified, for reasons that will become clear later.

With these preparations, we are now able to examine the topological properties of the system order by order. We first take $n = 2$ as an example with a sketched illustration in Fig. 1. Since k_1 is contained only in H_1 , and that the rest of the Hamiltonian anti-commutes with H_1 , a nontrivial $v_1(\mathbf{k}_{1,\parallel})$ indicates that the system support 1st-order boundary states at momentum $\mathbf{k}_{1,\parallel}$ under the open boundary condition (OBC) along r_1 -direction, whose eigenenergies are determined by H_2 [44, 45]. Furthermore, the bulk topological properties of H_2 can also be inherited by these 1st-order boundary states of H_1 , provided a BIS of H_2 (i.e. S_2^m) falls in the regime with a nontrivial v_1 [34]. In this way, 1st-order topology of

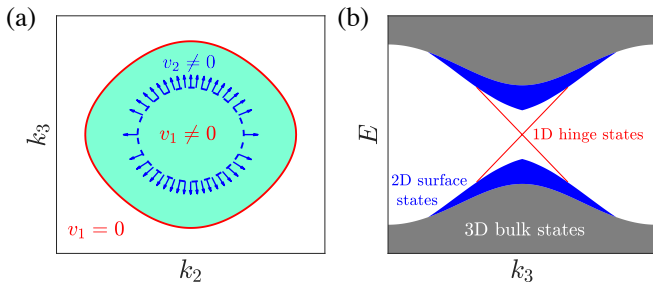


Figure 1. (color online). (a) An illustration of nested BISs for a 3D second-order topological phase. Here the red solid (blue dash) loop indicates the BIS $S_1^{m=2}$ ($S_2^{m=1}$), and the blue arrows is the normalized pseudospin texture along $S_2^{m=1}$ for H_2 (as in Eq. (2) with $n = 2$). (b) An illustration of corresponding energy spectrum, with OBCs aken along r_1 - and r_2 -directions of the system.

H_2 is manifested as 2nd-order topology of $H = H_1 + H_2$, and the system supports 2nd-order topological boundary states characterized by both v_1 and v_2 . In the example in Fig. 1(a), $S_2^{m=1}$ (blue dash loop) is “nested” in the regime with a nontrivial v_1 (green area) bounded by $S_1^{m=2}$ (red loop), and the pseudo-spin texture exhibits a nontrivial winding along $S_2^{m=1}$ (blue arrows), described by a winding number v_2 . Consequently, 1D chiral-like hinge states will appear in this 3D system under the OBC, as illustrated in Fig. 1(b).

In the above procedure, introducing the 2-BIS $S_1^{m=2}$ reduces both the dimension and the order of topology by 1 for the effective Hamiltonian $H - H_1 = H_2$. In other words, the 1st-order topology of H_2 is captured by the 1st-order surface states of H_1 , thus give rise to 2nd-order topological boundary states of the overall system. For $n > 2$, this procedure can be repeatedly applied to the Hamiltonian, until a 1st-order topological Hamiltonian H_n is obtained. For example, for $n = 3$, the 1st-order topology of H_3 is captured by the 1st-order surface states of H_2 , and the resultant 2nd-order topology of this subsystem is further captured by the 1st-order surface states of H_1 , leading to 3rd-order topological boundary states of the overall system. The inheritance of the topology only requires each S_i^m falls within the nontrivial regime associated with S_{i-1}^m . Finally, since the order of topology cannot be further reduced, the last BIS S_n^m is defined only for topologically characterize H_n and is not restricted to a 2nd-order one.

III. CLASSIFICATION OF HIGHER-ORDER TOPOLOGICAL PHASES WITH Z-INVARIANTS

Based on the time-reversal, particle-hole, and chiral symmetries, the tenfold AZ classification provides a systematic scheme for analyzing various topological properties. In this section, we focus on AZ classes with Z-type topological invariants, and construct corresponding continuous Hamiltonians for HOTPs in the form of Eq. (2).

We will first give a brief overview of the two complex classes (AIII and A) discussed in Ref. [34], then analysis the other eight real classes in more details. This analysis allows us to further generate lattice models of HOTPs characterized by the nested BISs in different classes, with examples given in Sec IV.

A. Higher-order topological phases for the complex symmetry classes

The nested-BIS method requires the Hamiltonian to satisfy Clifford algebra, which naturally leads to the presence or absence of the Chiral symmetry,

$$\mathcal{S}H(\mathbf{k})\mathcal{S}^{-1} = -H(\mathbf{k}) \quad (4)$$

with \mathcal{S} an unitary operator, and the system falls into the two complex symmetry classes AIII and A respectively. To see this, consider the Hamiltonian of Eqs. (1) and (2), which requires $d + n$ operators γ_j from Clifford algebra to generate d D n -th HOTPs. These operators can be given by the Kronecker product of p sets of Pauli matrices and the 2×2 identity matrix, which generates a set of $2^p \times 2^p$ matrices, where at most $2p + 1$ of them anti-commute with each other. Therefore, for $d + n = 2p$, there is one extra term absent in the Hamiltonian, acting as the chiral symmetry operator \mathcal{S} for the system; and for $d + n = 2p + 1$, no such a symmetry operator can be defined, unless some extra degrees of freedom is introduced to the system (which increases the dimension of the Hamiltonian matrix). Note that in these two classes, there is no further restriction of the exact coefficients of γ_j , since the chiral symmetry does not involve different momenta \mathbf{k} .

In our construction of the Hamiltonian in Eq. (2), we can calculate the winding number v_i with $i = 1, 2, \dots, n-1$ for every two-component subsystem H_i through Eq. (3). The last effective $(d - n + 1)$ D Hamiltonian H_n contains $(d - n + 2)$ anti-commuting terms, meaning it describes either an odd-dimensional system of class AIII with a chiral symmetry, or an even-dimensional system of class A without a chiral symmetry, both support Z-type 1st-order topology [35–38]. Therefore another Z-class topological invariant v_n can be defined through the spin texture at a BIS of H_n . As discussed in Sec II, nontrivial HOTPs are induced when the BISs of these Hamiltonian form the nesting relation, thus these HOTPs can be characterized by these n Z-class topological invariants, indexed as Z^n , which also corresponds to the number of boundary states at a n -th boundary. We emphasize that for even n , AIII (A) class can hold HOTPs in even (odd) dimension, which is topologically trivial in the conventional topological band theory. The classification and topological invariants of second-order topological phases for the two complex classes are shown in the first two rows of Table I.

Table I. Classification of second-order topological phases based on the nested-BIS method, according to the presence or absence of time-reversal, particle-hole, and chiral symmetries, labeled by \mathcal{T} , \mathcal{C} , and \mathcal{S} respectively in the table. “ \pm ” represents different types of anti-unitary symmetries square to ± 1 . The continuous Hamiltonians for topological phases characterized by two Z -invariants are provided with $H^{(I)}$ in Eq. (11), $H^{(II)}$ in Eq. (13), $H^{(III)}$ in Eq. (17), and $H^{(IV)}$ in Eq. (18). Note that in order to support second-order topology and corresponding boundary states in a lattice model, the spatial dimension must be $d \geq 2$.

Class	Symmetry			Dimension $d \pmod{8}$							
	\mathcal{T}	\mathcal{C}	\mathcal{S}	0	1	2	3	4	5	6	7
A	0	0	0	0	$Z \times Z$	0	$Z \times Z$	0	$Z \times Z$	0	$Z \times Z$
AIII	0	0	1	$Z \times Z$	0	$Z \times Z$	0	$Z \times Z$	0	$Z \times Z$	0
AI	+	0	0	$Z \times Z_2$	$Z \times Z$ $H^{(I)}$	0	0	0	$2Z \times Z$ $H^{(III)}$	0	$Z \times Z_2$
BDI	+	+	1	$Z \times Z_2$	$Z \times Z_2$	$Z \times Z$ $H^{(II)}$	0	0	0	$2Z \times Z$ $H^{(IV)}$	0
D	0	+	0	0	$Z \times Z_2$	$Z \times Z_2$	$Z \times Z$ $H^{(I)}$	0	0	0	$2Z \times Z$ $H^{(III)}$
DIII	−	+	1	$2Z \times Z$ $H^{(IV)}$	0	$Z \times Z_2$	$Z \times Z_2$	$Z \times Z$ $H^{(II)}$	0	0	0
AII	−	0	0	0	$2Z \times Z$ $H^{(III)}$	0	$Z \times Z_2$	$Z \times Z_2$	$Z \times Z$ $H^{(I)}$	0	0
CII	−	−	1	0	0	$2Z \times Z$ $H^{(IV)}$	0	$Z \times Z_2$	$Z \times Z_2$	$Z \times Z$ $H^{(II)}$	0
C	0	−	0	0	0	0	$2Z \times Z$ $H^{(III)}$	0	$Z \times Z_2$	$Z \times Z_2$	$Z \times Z$ $H^{(I)}$
CI	+	−	1	$Z \times Z$ $H^{(II)}$	0	0	0	$2Z \times Z$ $H^{(IV)}$	0	$Z \times Z_2$	$Z \times Z_2$

B. Second-order topological phases for the real classes

We now consider the HOTPs in real AZ symmetry classes described by integer topological invariant, and HOTPs containing Z_2 -invariant will be discussed in Sec V. A Hamiltonian in these classes holds time-reversal symmetry \mathcal{T} and/or particle-hole symmetry \mathcal{C} , with

$$\mathcal{T}H(\mathbf{k})\mathcal{T}^{-1} = H(-\mathbf{k}), \quad \mathcal{C}H(\mathbf{k})\mathcal{C}^{-1} = -H(-\mathbf{k}). \quad (5)$$

These anti-unitary symmetries have symmetry operators square to $+1$ or -1 , giving rise to $3^2 - 1 = 8$ real symmetry classes in total. In this subsection, we explore the classification of second-order topological phases and corresponding continuous Hamiltonian.

To study the Hamiltonian with anti-unitary symmetry conveniently, we define the $2p+1$ anti-commuting $2^p \times 2^p$ matrices from Clifford algebra as

$$\begin{aligned} \Gamma_{(2p+1)}^{2a-1} &= \underbrace{\sigma_z \otimes \dots \otimes \sigma_z}_{a-1} \otimes \sigma_x \otimes \underbrace{\sigma_0 \otimes \dots \otimes \sigma_0}_{p-a}, \\ \Gamma_{(2p+1)}^{2a} &= \underbrace{\sigma_z \otimes \dots \otimes \sigma_z}_{a-1} \otimes \sigma_y \otimes \underbrace{\sigma_0 \otimes \dots \otimes \sigma_0}_{p-a}, \\ \Gamma_{(2p+1)}^{2p+1} &= \sigma_z \otimes \sigma_z \dots \otimes \sigma_z \otimes \sigma_z \otimes \sigma_z \dots \otimes \sigma_z \end{aligned} \quad (6)$$

with $a = 1, 2, \dots, p$. In this representation, $\Gamma_{(2p+1)}^\alpha$ is purely real (imaginary) when α is odd (even), similar to the one used in Ref. [37]. Thus a anti-unitary operator can be defined as

$$\hat{A}_0 := \Pi_{\alpha=0}^p \Gamma_{(2p+1)}^{2\alpha+1} \mathcal{K} \quad (7)$$

where \mathcal{K} is the complex conjugate operator. For a Hamiltonian formed by the matrices in Eq. (6), \hat{A}_0 represents different symmetries (\mathcal{T} or \mathcal{C} with \pm in Table I) for different values of p , as it satisfies

$$\begin{aligned} \hat{A}_0^2 &= (-1)^{p(p+1)/2}, \\ \hat{A}_0 \Gamma_{(2p+1)}^\alpha \hat{A}_0^{-1} &= (-1)^p \Gamma_{(2p+1)}^\alpha. \end{aligned} \quad (8)$$

1. Gapless Hamiltonian as a starting point

We begin by writing down a $(2p+1)$ D gapless Dirac Hamiltonian,

$$H^{(0)}(\mathbf{k}) = \sum_{\alpha=1}^{2p+1} k_\alpha \Gamma_{(2p+1)}^\alpha. \quad (9)$$

It satisfies an anti-unitary symmetry

$$\hat{A}_0 H^{(0)}(\mathbf{k}) \hat{A}_0^{-1} = (-1)^{p+1} H^{(0)}(-\mathbf{k}), \quad (10)$$

which represents the time-reversal (particle-hole) symmetry when p is odd (even). The symmetry class of $H^{(0)}(\mathbf{k})$ is determined by further considering the square of \hat{A}_0 calculated through Eq. (8). That is, when p changes from 0 to 3, we got a series of odd-dimensional Hamiltonians with symmetry classes $D \rightarrow \text{AII} \rightarrow C \rightarrow \text{AI}$, with an eightfold periodicity of the spatial dimension $d = 2p + 1$.

2. Second-order Z-class Hamiltonian without chiral symmetry

Starting from the $(2p+1)$ D gapless Dirac Hamiltonian in Eq. (9), a $(2p)$ D gapped phase can be obtained by replacing one momentum component with a mass term m_1 . Nontrivial 1st-order topology may arise if m_1 takes different signs at different high-symmetric points and generate nontrivial winding of the Hamiltonian vector throughout the $(2p)$ D Brillouin zone. On the other hand, a Hamiltonian in the form of Eq. (2) supporting second-order topological phases can be divided into two subsystems with nontrivial 1st-order topology. Therefore we convert two terms with real matrices from Eq. (9) to mass terms ($k_1 \rightarrow m_1$ and $k_3 \rightarrow m_2$) and rewrite the resultant $(2p-1)$ D Hamiltonian as $H^{(I)}(\mathbf{k}) = H_1^{(I)}(\mathbf{k}) + H_2^{(I)}(\mathbf{k})$

$$\begin{aligned} H_1^{(I)}(\mathbf{k}) &= m_1 \Gamma_{(2p+1)}^1 + k_1 \Gamma_{(2p+1)}^2, \\ H_2^{(I)}(\mathbf{k}_{1,\parallel}) &= m_2 \Gamma_{(2p+1)}^3 + \sum_{\alpha=2}^{2p-1} k_\alpha \Gamma_{(2p+1)}^{\alpha+2}. \end{aligned} \quad (11)$$

Note the momentum components are reindexed to have α ranging from 1 to $2p-1$ for k_α . The anti-unitary symmetry of Eq. (7) is broken by these mass terms, but another one emerges for the system, given by

$$\begin{aligned} \hat{A}_1 H^{(I)}(\mathbf{k}) \hat{A}_1^{-1} &= (-1)^{p-1} H^{(I)}(-\mathbf{k}), \\ \hat{A}_1^2 &= (-1)^{(p-1)(p-2)/2}, \end{aligned} \quad (12)$$

where $\hat{A}_1 = \Gamma_{(2p+1)}^3 \Gamma_{(2p+1)}^1 \hat{A}_0$. It is straightforward to see that \hat{A}_1 also represents different symmetries for different p , and the corresponding symmetry class changes periodically as $\text{AI} \rightarrow \text{D} \rightarrow \text{AII} \rightarrow \text{C}$ when p increases from 1 to 4, as shown in Table I.

To unveil the topological characterization of $H^{(I)}(\mathbf{k})$, note that $H_1^{(I)}(\mathbf{k})$ can be viewed as a 1D Hamiltonian of k_1 , whose lattice counterpart can be characterized by a winding number defined as in Eq. (3). Meanwhile, $H_2^{(I)}(\mathbf{k}_{1,\parallel})$ is a $(2p-2)$ D Hamiltonian with $(2p-1)$ anti-commuting terms, belonging to the same symmetry class as that of $H^{(I)}(\mathbf{k})$ since they share the same symmetry conditions [46]. According to the standard AZ class, this $H_2^{(I)}(\mathbf{k}_{1,\parallel})$ is also characterized by a Z invariant. Thus the total system $H^{(I)}(\mathbf{k})$ is characterized two Z invariants, indexed as $Z \times Z$ in Table I.

3. Second-order Z-class Hamiltonian with chiral symmetry

The Hamiltonian in Eq. (11) includes a full set of $2^p \times 2^p$ anti-commuting matrices defined in Eq. (6), which excludes chiral symmetry for the system. To construct a chiral-symmetric Hamiltonian, we remove another term $k_{2p-1} \Gamma_{(2p+1)}^{2p+1}$ from Eq. (11), and obtain a $(2p-2)$ D Hamil-

tonian $H^{(II)}(\mathbf{k}) = H_1^{(II)}(\mathbf{k}) + H_2^{(II)}(\mathbf{k}_{1,\parallel})$, with

$$\begin{aligned} H_1^{(II)}(\mathbf{k}) &= m_1 \Gamma_{(2p+1)}^1 + k_1 \Gamma_{(2p+1)}^2, \\ H_2^{(II)}(\mathbf{k}_{1,\parallel}) &= m_2 \Gamma_{(2p+1)}^3 + \sum_{\alpha=2}^{2p-2} k_\alpha \Gamma_{(2p+1)}^{\alpha+2}. \end{aligned} \quad (13)$$

This Hamiltonian exhibits the same anti-unitary symmetry of \hat{A}_1 in Eq. (12), and also a chiral symmetry as the $\Gamma_{(2p+1)}^{2p+1}$ term is removed,

$$\Gamma_{(2p+1)}^{2p+1} H^{(II)}(\mathbf{k}) \Gamma_{(2p+1)}^{2p+1} = -H^{(II)}(\mathbf{k}). \quad (14)$$

Combining these two symmetries, another anti-unitary symmetry arises for the system,

$$\begin{aligned} \hat{A}_2 H^{(II)}(\mathbf{k}) \hat{A}_2^{-1} &= (-1)^p H^{(II)}(-\mathbf{k}), \\ \hat{A}_2^2 &= (-1)^{(p-2)(p-3)/2}, \end{aligned} \quad (15)$$

with

$$\hat{A}_2 = \Gamma_{(2p+1)}^{2p+1} \hat{A}_1. \quad (16)$$

When p increases from 1 to 4, the symmetry class for this $(2p-2)$ D Hamiltonian will change in the sequence of $\text{CI} \rightarrow \text{BDI} \rightarrow \text{DIII} \rightarrow \text{CII}$, as shown in Table I. Similarly to the previous case, here $H_1^{(II)}(\mathbf{k})$ is associated with a 1D winding topology, and $H_2^{(II)}(\mathbf{k}_{1,\parallel})$ corresponds to a $(2p-3)$ D system of the same symmetry class as $H^{(II)}(\mathbf{k})$, which is characterized by a Z invariant. Therefore the overall Hamiltonian also possesses $Z \times Z$ -type 2nd-order topology.

4. Second-order 2Z-class Hamiltonian without chiral symmetry

So far we have constructed Hamiltonians for two classes (one real and one complex) in each spatial dimension, where the second-order topology stems from the hybridization of a 1D winding topology and a 1st-order Z -type topology of the effective Hamiltonian $H_2(\mathbf{k}_{1,\parallel})$ in the same symmetry class but with one spatial dimension less than the total system. Based on the standard AZ classification, there is another class with 1st-order topology characterized by $2Z$ invariant in every spatial dimension [37], which can also be used to build higher-order topological phases.

To construct such a second-order $2Z$ -class Hamiltonian in the absence of chiral symmetry, we replace four terms of the gapless Hamiltonian of Eq. (9), $k_\alpha \Gamma_{2n+1}^\alpha$ with $\alpha = 1, 2, 3, 5$, with two mass terms $-im_1 \Pi_{\alpha=1}^3 \Gamma_{2n+1}^\alpha$ and $m_2 \Gamma_{2n+1}^5$, and obtain a gapped $(2p-3)$ D Hamiltonian $H^{(III)}(\mathbf{k}) = H_1^{(III)}(\mathbf{k}) + H_2^{(III)}(\mathbf{k}_{1,\parallel})$, with

$$\begin{aligned} H_1^{(III)}(\mathbf{k}) &= -im_1 \Pi_{\alpha=1}^3 \Gamma_{(2p+1)}^\alpha + k_1 \Gamma_{(2p+1)}^4, \\ H_2^{(III)}(\mathbf{k}_{1,\parallel}) &= m_2 \Gamma_{(2p+1)}^5 + \sum_{\alpha=2}^{2p-3} k_\alpha \Gamma_{(2p+1)}^{\alpha+4} \end{aligned} \quad (17)$$

with k_α reindexed from k_1 to k_{2p-3} . This Hamiltonian holds an anti-unitary symmetry

$$\hat{A}_3 = \Gamma_{(2p+1)}^5 \hat{A}_0$$

with

$$\begin{aligned} \hat{A}_3 H^{(III)}(\mathbf{k}) \hat{A}_3^{-1} &= (-1)^p H^{(III)}(-\mathbf{k}), \\ \hat{A}_3^2 &= (-1)^{p(p-1)/2}. \end{aligned}$$

When p changes from 2 to 5, this $(2p-3)$ D Hamiltonian's symmetry class changes as AII \rightarrow C \rightarrow AI \rightarrow D as shown in Table I.

To unveil the topological properties of this Hamiltonian, notice that the extra unitary matrix introduced for the first mass term satisfies $-i\Pi_{\alpha=1}^3 \Gamma_{2n+1}^\alpha = \sigma_0 \otimes \Gamma_{(2p-1)}^1$. Thus we rewrite the Hamiltonian of Eq. (17) as

$$\begin{aligned} H_1^{(III)}(\mathbf{k}) &= m_1 \sigma_0 \otimes \Gamma_{(2p-1)}^1 + k_1 \sigma_z \otimes \Gamma_{(2p-1)}^2, \\ H_2^{(III)}(\mathbf{k}_{1,\parallel}) &= m_2 \sigma_z \otimes \Gamma_{(2p-1)}^3 + \sum_{\alpha=2}^{2p-3} k_\alpha \sigma_z \otimes \Gamma_{(2p-1)}^{\alpha+2}, \end{aligned}$$

which can be reduced to the direct sum of two $H^{(I)}$ -type Hamiltonians in a $2^{p-1} \times 2^{p-1}$ Hilbert space,

$$\begin{aligned} H_{2^p \times 2^p}^{(III)}(\mathbf{k}) &= H_{2^{p-1} \times 2^{p-1}}^{(I)}(\mathbf{k}, m_1, m_2) \\ &\oplus H_{2^{p-1} \times 2^{p-1}}^{(I)}(-\mathbf{k}, m_1, -m_2). \end{aligned}$$

In addition, the two $H^{(I)}$ -type Hamiltonians can be mapped to each other through a unitary transformation, $\Gamma_{(2p-1)}^1 H_{2^{p-1} \times 2^{p-1}}^{(I)}(\mathbf{k}, m_1, m_2) \Gamma_{(2p-1)}^1 = H_{2^{p-1} \times 2^{p-1}}^{(I)}(-\mathbf{k}, m_1, -m_2)$. Consequently, the original Hamiltonian $H^{(III)}(\mathbf{k})$ possesses two copies of the $Z \times Z$ -type 2nd-order topology of $H^{(I)}(\mathbf{k})$, indexed as $2Z \times Z$ in Table I.

5. Second-order $2Z$ -class Hamiltonian with chiral symmetry

Finally, by removing $k_{2p-3} \Gamma_{(2p+1)}^{2p+1}$ from Hamiltonian (17), we can obtain a $(2p-3)$ D second-order $2Z$ -class Hamiltonian $H^{(IV)}(\mathbf{k}) = H_1^{(IV)}(\mathbf{k}) + H_2^{(IV)}(\mathbf{k}_{1,\parallel})$ with chiral symmetry,

$$\begin{aligned} H_1^{(IV)}(\mathbf{k}) &= -im_1 \Pi_{\alpha=1}^3 \Gamma_{(2p+1)}^\alpha + k_1 \Gamma_{(2p+1)}^4, \\ H_2^{(IV)}(\mathbf{k}_{1,\parallel}) &= m_2 \Gamma_{(2p+1)}^5 + \sum_{\alpha=2}^{2p-4} k_\alpha \Gamma_{(2p+1)}^{\alpha+4}. \end{aligned} \quad (18)$$

Obviously, this Hamiltonian keeps the anti-unitary symmetry of \hat{A}_3 in Eq. (18) and the same chiral symmetry as in Eq. (14), and their combination gives rise to another anti-unitary symmetry

$$\begin{aligned} \hat{A}_4 H^{(IV)}(\mathbf{k}) \hat{A}_4^{-1} &= (-1)^{p-1} H^{(IV)}(-\mathbf{k}), \\ \hat{A}_4^2 &= (-1)^{(p-1)(p-2)/2} \end{aligned}$$

with

$$\hat{A}_4 = \Gamma_{(2p+1)}^{2p+1} \hat{A}_3.$$

When p changes from 2 to 5, the symmetry class of this $(2p-4)$ D Hamiltonian changes in the sequence of DIII \rightarrow CII \rightarrow CI \rightarrow BDI, as shown in Table I. Similar to the previous discussion of $H^{(III)}(\mathbf{k})$, $H^{(IV)}(\mathbf{k})$ can be reduced to two copies of $H^{(II)}(\mathbf{k})$ in a (2^{p-1}) D Hilbert space, and thus possesses $2Z \times Z$ -type 2nd-order topology.

C. General higher-order topological phases with Z invariants for the real classes

Similarly, higher-order topological phases with an arbitrary order of topology can be obtained from the gapless Hamiltonian (9) through converting different terms with real matrices into mass terms. Here we list the general forms of Hamiltonians with higher-order topological phases:

- $(2p-n+1)$ D higher-order Z -class Hamiltonian without chiral symmetry:

$$\begin{aligned} H_1^{(I)}(\mathbf{k}) &= m_1 \Gamma_{(2p+1)}^1 + k_1 \Gamma_{(2p+1)}^2, \\ H_2^{(I)}(\mathbf{k}_{1,\parallel}) &= m_2 \Gamma_{(2p+1)}^3 + k_2 \Gamma_{(2p+1)}^4, \\ &\dots \\ H_{n-1}^{(I)}(\mathbf{k}_{n-2,\parallel}) &= m_{n-1} \Gamma_{(2p+1)}^{2n-3} + k_{n-1} \Gamma_{(2p+1)}^{2n-2}, \\ H_n^{(I)}(\mathbf{k}_{n-1,\parallel}) &= m_n \Gamma_{(2p+1)}^{2n-1} + \sum_{\alpha=n}^{2p-n+1} k_\alpha \Gamma_{(2p+1)}^{n+\alpha}; \end{aligned} \quad (19)$$

- $(2p-n)$ D higher-order Z -class Hamiltonian with chiral symmetry:

$$\begin{aligned} H_1^{(II)}(\mathbf{k}) &= m_1 \Gamma_{(2p+1)}^1 + k_1 \Gamma_{(2p+1)}^2, \\ H_2^{(II)}(\mathbf{k}_{1,\parallel}) &= m_2 \Gamma_{(2p+1)}^3 + k_2 \Gamma_{(2p+1)}^4, \\ &\dots \\ H_{n-1}^{(II)}(\mathbf{k}_{n-2,\parallel}) &= m_{n-1} \Gamma_{(2p+1)}^{2n-3} + k_{n-1} \Gamma_{(2p+1)}^{2n-2}, \\ H_n^{(II)}(\mathbf{k}_{n-1,\parallel}) &= m_n \Gamma_{(2p+1)}^{2n-1} + \sum_{\alpha=n}^{2p-n} k_\alpha \Gamma_{(2p+1)}^{n+\alpha}; \end{aligned} \quad (20)$$

- $(2p-n-1)$ D higher-order $2Z$ -class Hamiltonian without chiral symmetry:

$$\begin{aligned} H_1^{(III)}(\mathbf{k}) &= -im_1 \Pi_{\alpha=1}^3 \Gamma_{(2p+1)}^\alpha + k_1 \Gamma_{(2p+1)}^4, \\ H_2^{(III)}(\mathbf{k}_{1,\parallel}) &= m_2 \Gamma_{(2p+1)}^5 + k_2 \Gamma_{(2p+1)}^6, \\ &\dots \\ H_{n-1}^{(III)}(\mathbf{k}_{n-2,\parallel}) &= m_{n-1} \Gamma_{(2p+1)}^{2n-1} + k_{n-1} \Gamma_{(2p+1)}^{2n}, \\ H_n^{(III)}(\mathbf{k}_{n-1,\parallel}) &= m_n \Gamma_{(2p+1)}^{2n+1} + \sum_{\alpha=n}^{2p-n-1} k_\alpha \Gamma_{(2p+1)}^{n+\alpha+2}; \end{aligned} \quad (21)$$

- $(2p - n - 2)$ D higher-order $2Z$ -class Hamiltonian with chiral symmetry:

$$\begin{aligned}
H_1^{(IV)}(\mathbf{k}) &= -im_1 \Pi_{\alpha=1}^3 \Gamma_{(2p+1)}^\alpha + k_1 \Gamma_{(2p+1)}^4, \\
H_2^{(IV)}(\mathbf{k}_{1,\parallel}) &= m_2 \Gamma_{(2p+1)}^5 + k_2 \Gamma_{(2p+1)}^6, \\
&\dots \\
H_{n-1}^{(IV)}(\mathbf{k}_{n-2,\parallel}) &= m_{n-1} \Gamma_{(2p+1)}^{2n-1} + k_{n-1} \Gamma_{(2p+1)}^{2n}, \\
H_n^{(IV)}(\mathbf{k}_{n-1,\parallel}) &= m_n \Gamma_{(2p+1)}^{2n+1} + \sum_{\alpha=n}^{2p-n-2} k_\alpha \Gamma_{(2p+1)}^{n+\alpha+2}. \quad (22)
\end{aligned}$$

Among these Hamiltonians, those in Eqs. (19) and (20) can be characterized by n Z -class invariant and indexed by Z^n . Each of the rest two Hamiltonians in Eqs. (21) and (22) can be reduced to two Z -class Hamiltonians, and is indexed by $2Z^n$. Obviously, these results with $n = 1$ recovers conventional (1st-order) topological phases, and previous results of 2nd-order topological phases can be recovered by setting $n = 2$. Note that when the order of topology n increases by one and p remains the same, the spatial dimension d decreases by one for the above Hamiltonians, shifting all topological indexes one column to the left in the symmetry classification table. Meanwhile, as detailed in Appendix A, particle-hole symmetry with $\mathcal{C}^2 = \pm 1$ will convert to time-reversal symmetry with $\mathcal{T}^2 = \pm 1$, and time-reversal symmetry with $\mathcal{T}^2 = \pm 1$ becomes particle-hole symmetry with $\mathcal{C}^2 = \mp 1$, shifting all topological indexes up two rows in the symmetry classification table. Putting these results together, the AZ classification table for $(n+1)$ th-order topological phases can be obtained from that for n th-order topological phases by shifting all topological indexes up one row. A general classification table for topological phases with arbitrary orders of topology can be obtained accordingly, as given in Appendix A.

IV. LATTICE HAMILTONIAN AND EXAMPLES

After obtaining the continuous Hamiltonian, we now provide some specific lattice models to illustrate the HOTPs with nested BISs in 2D and 3D. Note that a continuous Hamiltonian can be considered as the low-energy expansion near high symmetric points of a lattice Hamiltonian. Explicitly, we apply the transformation:

$$\begin{aligned}
k_\alpha &\rightarrow h_\alpha(\mathbf{k}) := \sin k_\alpha, \\
m_\alpha &\rightarrow M_\alpha(\mathbf{k}) := m_\alpha + \sum_{i=\alpha}^d (1 - \cos k_i). \quad (23)
\end{aligned}$$

Then a minimum Hamiltonian with nearest neighbor hoppings and unitary topological charges belonging to a certain symmetry class is obtained. For simplicity but without loss of generality, we consider the regime with $|m_i| < 2$, where the Hamiltonian has band inversion at

$\mathbf{k} = 0$. The low-energy expansion of lattice Hamiltonian near $\mathbf{k} = 0$ is the corresponding continuous Hamiltonian. We will provide several examples and display their topological properties in this section.

A. Examples: 3D and 2D Z -class second-order topological phases

To begin with, we illustrate two examples of 2nd-order topological phases, namely a D class 3D Hamiltonian and a BDI class 2D Hamiltonian, obtained by applying the transformation of Eq. (23) to Hamiltonian $H^{(I)}(\mathbf{k})$ of Eq. (11) and Hamiltonian $H^{(II)}(\mathbf{k})$ of Eq. (13) respectively. The 3D Hamiltonian with 2nd-order topology in D class reads $H^{(D)}(\mathbf{k}) = H_1^{(D)}(\mathbf{k}) + H_2^{(D)}(\mathbf{k}_{1,\parallel})$, with

$$\begin{aligned}
H_1^{(D)}(\mathbf{k}) &= M_1(\mathbf{k}) \sigma_x \tau_0 + h_1(\mathbf{k}) \sigma_y \tau_0, \\
H_2^{(D)}(\mathbf{k}_{1,\parallel}) &= M_2(\mathbf{k}_{1,\parallel}) \sigma_z \tau_x + h_2(\mathbf{k}_{1,\parallel}) \sigma_z \tau_y \\
&\quad + h_3(\mathbf{k}_{1,\parallel}) \sigma_z \tau_z, \quad (24)
\end{aligned}$$

where $M_1 = m_1 + 3 - \cos k_1 - \cos k_2 - \cos k_3$, $M_2 = m_2 + 2 - \cos k_2 - \cos k_3$, $h_1 = \sin k_1$, $h_2 = \sin k_2$ and $h_3 = \sin k_3$. Here $\sigma_{\beta=x,y,z}$ and $\tau_{\beta=x,y,z}$ are two sets of Pauli matrices, and τ_0 is the two-by-two identity matrix. Following previous discussion, this Hamiltonian supports a particle-hole symmetry, $\mathcal{C}H^{(D)}(\mathbf{k})\mathcal{C}^{-1} = -H^{(D)}(-\mathbf{k})$ with $\mathcal{C} = \sigma_z \tau_z \mathcal{K}$ and $\mathcal{C}^2 = 1$.

Based on the nested-BIS method, we can define a nontrivial winding number $v_1(\mathbf{k}_{\parallel})$ along r_1 -direction for $H_1^{(D)}(\mathbf{k})$:

$$v_1(\mathbf{k}_{1,\parallel}) = \frac{1}{2\pi} \oint_{k_1} \frac{h_1 dM_1 - M_1 dh_1}{M_1^2 + h_1^2}. \quad (25)$$

The 2nd-BIS $S_1^{m=2}$ given by $H_1^{(D)}(\mathbf{k}) = 0$ acts as a boundary between nontrivial region with $v_1 \neq 0$ and trivial region with $v_1 = 0$, as shown in Fig. 2(a). According to the bulk-boundary correspondence, the nontrivial invariant $v_1 \neq 0$ corresponds to the appearance of surface states in the (100) and $(\bar{1}00)$ surface. We then define a 1st-BIS $S_2^{m=1}$ of $H_2^{(D)}(\mathbf{k})$ in the 2D BZ of $\mathbf{k}_{1,\parallel}$ as the area with $M_2(\mathbf{k}_{1,\parallel}) = 0$. When $S_2^{m=1}$ falls within the region with nontrivial $v_1 \neq 0$, the topological properties of the Hamiltonian $H_2^{(D)}(\mathbf{k}_{1,\parallel})$ can be captured by these surface states [34]. Then we obtain an effective 2D Hamiltonian in the subspace associated with each surface state [7, 8]:

$$\begin{aligned}
H_{\text{eff},\pm}^{(D)} &= P_{1,\pm} H_2^{(D)} P_{1,\pm} \\
&= P_{1,\pm} (M_2 \sigma_z \tau_x + h_2 \sigma_z \tau_y + h_3 \sigma_z \tau_z) P_{1,\pm}, \\
P_{1,\pm} &= [1 \pm i(\sigma_y \tau_0)(\sigma_x \tau_0)]/2 = (1 \pm \sigma_z \tau_0)/2, \quad (26)
\end{aligned}$$

where $P_{1,+}$ and $P_{1,-}$ indicate the projection operators onto the subspace of low-energy surface states on (100) and $(\bar{1}00)$ surfaces, respectively. Therefore the surface states share the same topological properties with $H_2^{(D)}$,

whose nontrivial topology gives rise to 2nd-order surface states of the parent 3D system.

To topologically characterize $H_2^{(D)}(\mathbf{k}_{1,\parallel})$, a winding number can be defined for the pseudo-spin texture of (h_2, h_3) along the 1st-BIS $S_2^{m=1}$,

$$v_2 = \frac{1}{2\pi} \int_{S_2^{m=1}} d\theta \quad (27)$$

with $\theta = \arctan(h_3/h_2)$, which is equivalent to the Chern number defined in the 2D BZ [41, 47]. Chiral-like hinge

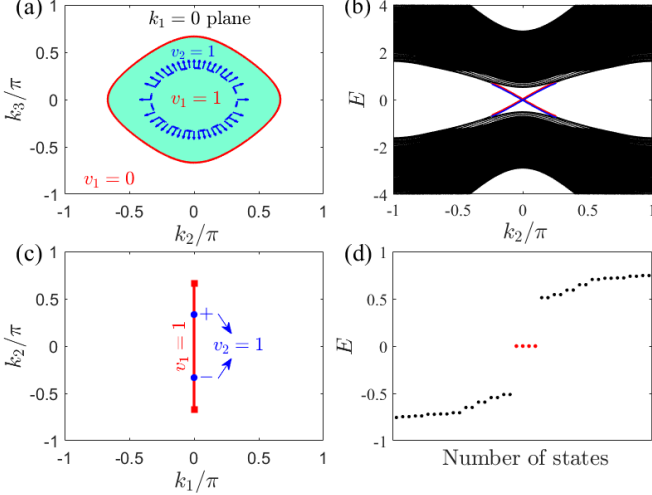


Figure 2. (color online). (a) Nested BISs for Hamiltonian $H^{(D)}(\mathbf{k})$ of Eq. (24), where $S_1^{m=2}$ and $S_2^{m=1}$ are indicated by the red solid loop and blue dashed loop, respectively. Blue arrows indicate the normalized vector of (h_2, h_3) . (b) Energy spectrum for Hamiltonian in Eq. (24) with PBC along r_3 -direction and OBCs for the other two directions. The hinge states on (100) and $(\bar{1}00)$ are indicated by red and blue lines respectively. (c) Nested BISs for Hamiltonian of Eq. (28). The red squares and blue dots indicate the BIS $S_1^{m=2}$ and $S_2^{m=1}$, respectively. Red line indicates the region of k_2 with $v_1 = 1$. (d) Eigenenergies for Hamiltonian of Eq. (28) with zero-energy corner states (red dots). In all panels $m_1 = -1.5$ and $m_2 = -0.5$ have been set.

states are seen when the two BISs are nested in the proper order, i.e. when $S_2^{m=1}$ falls within the region with nontrivial $v_1 \neq 0$ bounded by $S_1^{m=2}$ in the 2D BZ of (k_2, k_3) , as displayed in Fig. 2(b).

By removing terms associated with k_3 from the Hamiltonian (24) (or by transforming $H^{(II)}(\mathbf{k})$ in 2D into a lattice model), we can get a 2D Hamiltonian in BDI class $H^{(\text{BDI})}(\mathbf{k}) = H_1^{(\text{BDI})}(\mathbf{k}) + H_2^{(\text{BDI})}(\mathbf{k}_{1,\parallel})$ with

$$\begin{aligned} H_1^{(\text{BDI})}(\mathbf{k}) &= M_1(\mathbf{k})\sigma_x\tau_0 + h_1(\mathbf{k})\sigma_y\tau_0, \\ H_2^{(\text{BDI})}(\mathbf{k}_{1,\parallel}) &= M_2(\mathbf{k}_{1,\parallel})\sigma_z\tau_x + h_2(\mathbf{k}_{1,\parallel})\sigma_z\tau_y, \end{aligned} \quad (28)$$

where $M_1 = m_1 + 2 - \cos k_1 - \cos k_2$, $M_2 = m_2 + 1 - \cos k_2$, $h_1 = \sin k_1$ and $h_2 = \sin k_2$. In addition to the particle-hole symmetry $\mathcal{C} = \sigma_z\tau_z\mathcal{K}$, this Hamiltonian also holds a time-reversal symmetry: $\mathcal{T}H^{(\text{BDI})}(\mathbf{k})\mathcal{T}^{-1} = H^{(\text{BDI})}(-\mathbf{k})$

with $\mathcal{T} = \mathcal{K}$ and $\mathcal{T}^2 = 1$, and a chiral symmetry $\mathcal{S}H^{(\text{BDI})}(\mathbf{k})\mathcal{S}^{-1} = -H^{(\text{BDI})}(\mathbf{k})$ with $\mathcal{S} = \mathcal{C}\mathcal{T} = \sigma_z\tau_z$.

Similarly, the 2nd-BIS $S_1^{m=2}$ separate the k_2 axis into nontrivial region and trivial region, as shown in Fig. 2(c). The topological invariant of $H_2^{(\text{BDI})}(\mathbf{k})$ can be obtained through [42]

$$v_2 = \frac{1}{2} \sum_{S_2^{m=1}} \text{Sgn}\left[\frac{\partial M_2}{\partial k_2} h_2\right]. \quad (29)$$

where $S_2^{m=1}$ indicates the discrete points satisfying $M_2 = 0$. When $S_2^{m=1}$ falls within the region with $v_1 \neq 0$ bounded by $S_1^{m=2}$ in the 1D BZ of k_2 , the 0D corner states appear, as shown in Fig. 2(d).

For these two Hamiltonians, the topological invariants can be indexed as $Z \times Z$, i.e. the two parts of Hamiltonian can be indexed by Z -class topological invariants and second-order topological phases appear when their BISs satisfy the nested relation. It also establishes for all Hamiltonian $H^{(I)}$ of Eq. (11) and $H^{(II)}$ of Eq. (13), indexed as $Z \times Z$ in Table. I. The other two case, namely $H^{(III)}$ of Eq. (17) and $H^{(IV)}$ of Eq. (18), are indexed as $2Z \times Z$ in Table. I, as their BISs and pseudospin texture are similar to the first two classes but the number of topological boundary states will double, and an example will be given in the following subsection.

B. Examples: 3D Z -class and $2Z$ -class third-order topological phases

Next we give two 3D examples of 3rd-order topological phases with Z and $2Z$ invariants, by applying the transformation of Eq. (23) to Hamiltonian $H^{(I)}(\mathbf{k})$ of Eq. (19) and Hamiltonian $H^{(III)}(\mathbf{k})$ of Eq. (21) with $n = 3$ for both cases, respectively. The first one falls in the BDI class, described by the Hamiltonian $H^{(\text{BDI})}(\mathbf{k}) = H_1^{(\text{BDI})}(\mathbf{k}) + H_2^{(\text{BDI})}(\mathbf{k}_{1,\parallel}) + H_3^{(\text{BDI})}(k_3)$ with

$$\begin{aligned} H_1^{(\text{BDI})}(\mathbf{k}) &= M_1(\mathbf{k})\sigma_x\tau_0s_0 + h_1(\mathbf{k})\sigma_y\tau_0s_0, \\ H_2^{(\text{BDI})}(\mathbf{k}_{1,\parallel}) &= M_2(\mathbf{k}_{1,\parallel})\sigma_z\tau_xs_0 + h_2(\mathbf{k}_{1,\parallel})\sigma_z\tau_ys_0, \\ H_3^{(\text{BDI})}(k_3) &= M_3(k_3)\sigma_z\tau_zs_x + h_3(k_3)\sigma_z\tau_zs_y, \end{aligned} \quad (30)$$

where $M_1 = m_1 + 3 - \cos k_1 - \cos k_2 - \cos k_3$, $M_2 = m_2 + 2 - \cos k_2 - \cos k_3$, $M_3 = m_3 + 1 - \cos k_3$, $h_1 = \sin k_1$, $h_2 = \sin k_2$, and $h_3 = \sin k_3$. Here we have introduced another set of Pauli matrices indexed by $s_{x,y,z}$. This Hamiltonian satisfies a particle-hole symmetry $\mathcal{C} = \sigma_z\tau_zs_z\mathcal{K}$ with $\mathcal{C}^2 = 1$, a time-reversal symmetry $\mathcal{T} = \mathcal{K}$ with $\mathcal{T}^2 = 1$, and a chiral symmetry $\mathcal{S} = \mathcal{C}\mathcal{T} = \sigma_z\tau_zs_z$.

To apply the nested-BIS method, we can define three BISs as $S_1^{m=2} : H_1^{(\text{BDI})} = 0$, $S_2^{m=2} : H_2^{(\text{BDI})} = 0$ and $S_3^{m=1} : M_3 = 0$. Then when these BISs correspond to nontrivial topology and form nested relations [e.g., as shown in Fig. 3(a)], $Z \times Z \times Z$ corner states shall emerge at each corner, give rise to 8 in-gap topological states for a 3D system, as displayed in Fig. 3(b).

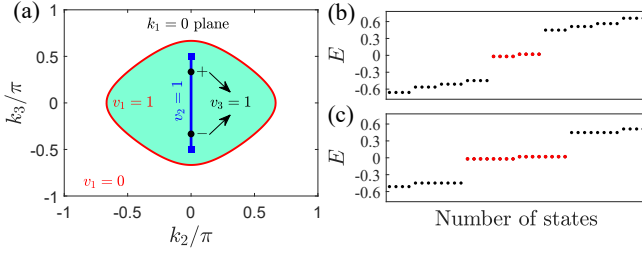


Figure 3. (color online). (a) Nested BISs for Hamiltonian $H^{(\text{BDI})}(\mathbf{k})$ of Eq. (30) and $H^{(\text{CII})}(\mathbf{k})$ of Eq. (31). Red loop, blue squares and black dots indicate $S_1^{m=2}$, $S_2^{m=2}$, and $S_3^{m=1}$ respectively. (b), (c) Energy spectra for $H^{(\text{BDI})}(\mathbf{k})$ of Eq. (30) and $H^{(\text{CII})}(\mathbf{k})$ of Eq. (31), respectively, where all three directions are under OBCs. Other parameters are $m_1 = -1.5$, $m_2 = -1$ and $m_3 = -0.5$ in all panels. Red dots represent topological corner states in these models, which acquire small nonzero energies due to finite-size effect ($8 \times 8 \times 8$ unit cells are considered in our calculation).

Similarly, substituting Eq. (23) to Hamiltonian of Eq. (21), we can get a 3D third-order topological phase in CII class $H^{(\text{CII})}(\mathbf{k}) = H_1^{(\text{CII})}(\mathbf{k}) + H_2^{(\text{CII})}(\mathbf{k}_{1,\parallel}) + H_3^{(\text{CII})}(k_3)$ with

$$\begin{aligned} H_1^{(\text{CII})}(\mathbf{k}) &= M_1(\mathbf{k})\sigma_0\tau_x s_0 s_0 + h_1(\mathbf{k})\sigma_z\tau_y s_0 s_0, \\ H_2^{(\text{CII})}(\mathbf{k}_{1,\parallel}) &= M_2(\mathbf{k}_{1,\parallel})\sigma_z\tau_z s_x s_0 + h_2(\mathbf{k}_{1,\parallel})\sigma_z\tau_z s_y s_0, \\ H_3^{(\text{CII})}(k_3) &= M_3(k_3)\sigma_z\tau_z s_z s_x + h_3(k_3)\sigma_z\tau_z s_z s_y, \end{aligned} \quad (31)$$

where the coefficients $M_{1,2,3}$ and $h_{1,2,3}$ are the same as those of Hamiltonian $H^{(\text{BDI})}(\mathbf{k})$ in Eq. (30), but another set of Pauli matrices $\varsigma_{x,y,z}$ has been introduced. This Hamiltonian holds a particle-hole symmetry $\mathcal{C} = i\sigma_x\tau_y s_z \varsigma_z \mathcal{K}$ with $\mathcal{C}^2 = -1$, a time-reversal symmetry $\mathcal{T} = i\sigma_y\tau_x s_0 \varsigma_0 \mathcal{K}$ with $\mathcal{T}^2 = -1$, and a chiral symmetry $\mathcal{S} = \mathcal{C}\mathcal{T} = \sigma_z\tau_z s_z \varsigma_z$. By definition, the BISs and their corresponding topological invariants of $H^{(\text{CII})}(\mathbf{k})$ are the same as those of $H^{(\text{BDI})}(\mathbf{k})$. The only difference is that the pseudospin space is doubled by the extra set of Pauli matrices, leading to double corner states at each corner, namely 16 in-gap topological states in the topologically nontrivial regime, as shown in Fig. 3(c). Thus the topological properties of this model are indexed as $2Z \times Z \times Z$.

V. HIGHER-ORDER TOPOLOGICAL PHASES WITH Z_2 TOPOLOGY

In this section, we derive HOTPs with Z_2 properties from two parent Hamiltonians indexed by Z^n , i.e. $H^{(I)}$ in Eq. (19) and $H^{(II)}$ in Eq. (20). That is, we convert the last subsystem H_n to a Z_2 -class Hamiltonian and keep the rest two-component parts in Eq. (2) unchanged. Then their topological invariants can be indexed as $Z^{n-1} \times Z_2$.

In particular for the symmetry class without chiral symmetry, the HOTPs with Z_2 properties can be obtained from the lattice Hamiltonian corresponding to $H^{(I)}$ in Eq. (19) through the conversion [48]:

$$\begin{aligned} H_n^{(I)}(\mathbf{k}_{n-1,\parallel}) &= M_n \Gamma_{(2p+1)}^{2n-1} + \sum_{\alpha=n}^{2p-n+1} h_\alpha \Gamma_{(2p+1)}^{n+\alpha} \\ &\Downarrow \\ H_n^{(I,s)}(\mathbf{k}_{n-1,\parallel}) &= M_n \Gamma_{(2p+1)}^{2n-1} + \sum_{\alpha=n}^{2p-n-s+1} h_\alpha \Gamma_{(2p+1)}^{n+\alpha} \\ &\quad + \sum_{\alpha=1}^s f_\alpha \Gamma_{(2p+1)}^{2p+2-\alpha}. \end{aligned} \quad (32)$$

And for the symmetry class with chiral symmetry, the HOTPs with Z_2 properties can be obtained from the lattice Hamiltonian corresponding to $H^{(II)}$ of Eq. (20) through the conversion [37]:

$$\begin{aligned} H_n^{(II)}(\mathbf{k}_{n-1,\parallel}) &= M_n \Gamma_{(2p+1)}^{2n-1} + \sum_{\alpha=n}^{2p-n} h_\alpha \Gamma_{(2p+1)}^{n+\alpha} \\ &\Downarrow \\ H_n^{(II,s)}(\mathbf{k}_{n-1,\parallel}) &= M_n \Gamma_{(2p+1)}^{2n-1} + \sum_{\alpha=n}^{2p-n-s} h_\alpha \Gamma_{(2p+1)}^{n+\alpha} \\ &\quad + \sum_{\alpha=1}^s f_\alpha \Gamma_{(2p+1)}^{2p+1-\alpha}. \end{aligned} \quad (33)$$

In Eqs. (32) and (33), $s = 1, 2$ indicates two descendants with Z_2 topology of $H^{(I)}$ or $H^{(II)}$, and f_α is chosen to be an odd function of the reduced momentum $\mathbf{k}_{n-1,\parallel}$. With these conversions, the first (second) descendant falls in the same symmetry class as its parent Hamiltonian, but with one (two) spatial dimension lower as one (two) momentum component is converted into f_α . The classification of these second-order topological phases with Z_2 property have also been listed in Table I.

We provide a 2D D class second-order topological phase as example, which is a first descendant of the lattice Hamiltonian of Eq. (24):

$$\begin{aligned} H^{(\text{D},1)}(\mathbf{k}) &= H_1^{(\text{D},1)}(\mathbf{k}) + H_2^{(\text{D},1)}(k_2), \\ H_1^{(\text{D},1)}(\mathbf{k}) &= M_1(\mathbf{k})\sigma_x\tau_0 + h_1(\mathbf{k})\sigma_y\tau_0, \\ H_2^{(\text{D},1)}(k_2) &= M_2(k_2)\sigma_z\tau_x + h_2(k_2)\sigma_z\tau_y + f_1(k_2)\sigma_z\tau_z, \end{aligned} \quad (34)$$

where $M_1 = m_1 + 2 - \cos k_1 - \cos k_2$, $M_2 = m_2 + 1 - \cos k_2 - \lambda_1 \cos(2k_2)$, $h_1 = \sin k_1$, $h_2 = \sin k_2$ and $f_1 = \sin(2k_2)$. Here we introduce next-nearest neighbor hopping to generate $2k_2$ terms for demonstrating its Z_2 properties [49].

Analogous to its parent Hamiltonian, we can define v_1 and a 2-BIS $S_1^{m=2}$ for $H_1^{(\text{D},1)}(\mathbf{k})$, and a first-order BIS (1-BIS) $S_2^{m=1}$ for $H_2^{(\text{D},1)}(k_2)$. When $S_2^{m=1}$ falls within the nontrivial region bounded by $S_1^{m=2}$, the boundary states of $H_1^{(\text{D},1)}(\mathbf{k})$ can capture the topology of $H_2^{(\text{D},1)}(k_2)$. But

we still need to check whether $H_2^{(D,1)}(k_2)$ is topologically nontrivial or not, which can be characterized by a Berry phase [50] or the dynamical invariant at its highest-order BISs [51]. In order to define a topological invariant of $H_2^{(D,1)}$ based on the BIS $S_2^{m=1}$, we introduce an auxiliary Hamiltonian

$$\tilde{H}_2^{(D,1)}(k_2, \theta) = \tilde{M}_2(k_2, \theta)\sigma_z\tau_x + h_2(k_2)\sigma_z\tau_y + \tilde{f}_1(k_2, \theta)\sigma_z\tau_z, \quad (35)$$

where $\tilde{M}_2(k_2, \theta) = M_2(k_2) + \lambda_2(1 - \cos \theta)$ and $\tilde{f}_1(k_2, \theta) = \sin(2k_2 + \theta)$. This Hamiltonian preserves the same symmetries as $H_2^{(D,1)}(k_2)$, and satisfies $\tilde{H}_2^{(D,1)}(k_2, 0) = H_2^{(D,1)}(k_2)$. On the other hand, provided λ_2 is large enough, $\tilde{H}_2^{(D,1)}(k_2, \theta = \pi)$ is topologically trivial, which is called the ‘vacuum’ projection. Therefore the topological difference between $H_2^{(D,1)}(k_2)$ and vacuum can be captured by a topological invariant \tilde{v}_2 defined for $\tilde{H}_2^{(D,1)}(k_2, \theta)$ in the 2D parameter space of (k_2, θ) [37, 48]. Finally, \tilde{v}_2 can be obtained along a 1-BIS of $\tilde{H}_2^{(D,1)}(k_2, \theta)$, $\tilde{S}_2^{m=1} : \tilde{M}_2(k_2, \theta) = 0$, which reproduces the 1-BIS $S_2^{m=1}$ of $H_2^{(D,1)}(k_2)$ at $\theta = 0$. The Z_2 invariant for $H_2^{(D,1)}(k_2)$ is thus defined as

$$v_2 = \text{mod}(\tilde{v}_2, 2),$$

which actually is independent from the details of interpolation between $\theta = 0$ and π , but only depends on $H_2^{(D,1)}(k_2)$. In Fig. 4(a), the two BISs of $H^{(D,1)}(\mathbf{k})$ in

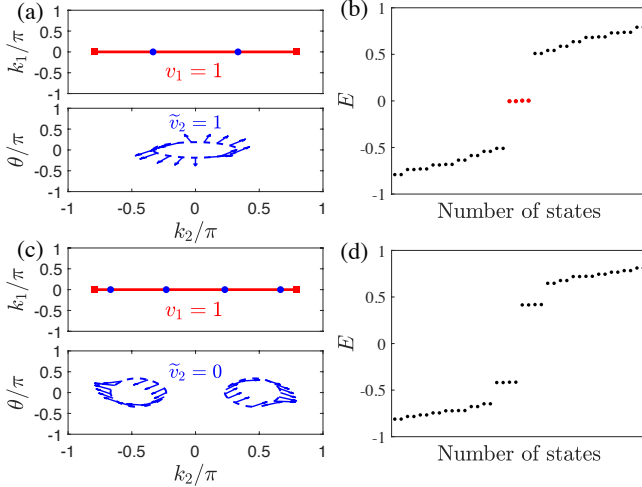


Figure 4. (color online). (a) Nested BISs for Hamiltonian $H^{(D,1)}(\mathbf{k})$ of Eq. (34) and the vector (h_2, \tilde{f}_1) of Eq. (35) (blue arrows, after normalization) along the BISs $\tilde{S}_2^{m=1}$ (dash loops), with $\lambda_1 = 0$. Here $S_1^{m=2}$ and $S_2^{m=1}$ are indicated by red squares and blue dots, respectively. (b) Corresponding eigenenergies closed to zero under OBCs. (c) and (d) demonstrate the same results as in (a) and (b), but with $\lambda_1 = -2$. Other parameters are $m_1 = -1.8$, $m_2 = -0.5$, and $\lambda_2 = 3$. Red dots in (b) indicate zero-energy corner states.

Eq. (34) form nested relation, and the topological invariant \tilde{v}_2 takes an odd value, so that $v_2 = 1$. As a result, four zero-energy corner states appear in the system, as displayed in Fig. 4(b).

In contrast, in Fig. 4(c) we illustrate another situation where $\tilde{v}_2 = 0$. The BIS $S_2^{m=1}$ also falls within the non-trivial region of v_1 , yet the system is topologically trivial as $v_2 = 0$. Consistently, the energy spectrum in Fig. 4(d) shows no zero-energy corner state in its band gap. We note that the value of \tilde{v}_2 may change when introducing a different $\tilde{H}_2^{(D,1)}(k_2, \theta)$, but its parity reminds the same and predicts the Z_2 invariant v_2 . An example with $\tilde{v}_2 = 2$ is given in Appendix B.

VI. ASYMMETRIC BOUNDARY STATES

In previous discussion, the higher-order topological boundary states are seen to distribute along spatially symmetric hinges (e.g., with a C_4 rotation symmetry in k_2 - k_3 plane) of 3D systems, and at the four corners of 2D systems. this is because the examples we consider are some minimal models with certain coincidental spatial symmetries, which are not necessary for constructing topological phases in the AZ classification. For example, higher-order topological corner states can emerge in 2D and 3D lattices without any spatial symmetry, which host corner states with different configurations [17]. In this section, we will extend our discussion to several scenarios with more sophisticated nested BISs, where asymmetric properties arise due to certain spatial-symmetry breaking. In particular, crossed BISs give rise to asymmetric behaviors in different directions on the same surfaces of a 3D system, while certain non-Clifford terms can induce boundary states asymmetric between two opposite surfaces [e.g., (100) and $(\bar{1}00)$].

A. Crossed band inversion surfaces

1. Asymmetric properties between k_2 and k_3

In the above sections, we have discussed several 3D systems where the BISs always enclose each other, which is ensured by a C_4 rotation symmetry in the k_2 - k_3 plane,

$$\mathcal{C}_4 H^{(D)}(k_1, k_2, k_3) \mathcal{C}_4^{-1} = H^{(D)}(k_1, -k_3, k_2) \quad (36)$$

with $\mathcal{C}_4 = e^{i\pi/4\sigma_0\tau_x}$. To go beyond this scenario, we consider a Hamiltonian similar to Eq. (24), but with an asymmetric parameter γ in M_2 :

$$M_2(\mathbf{k}_{\parallel}) = m_2 + (1 - \cos k_2) + \gamma(1 - \cos k_3). \quad (37)$$

Thus the C_4 rotation symmetry is broken, and the second BIS $S_2^{m=1}$ is deformed and crosses the other BIS $S_1^{m=2}$, as shown in Fig. 5(a).

To topologically characterize this asymmetric Hamiltonian with the nested-BIS method, we further define two

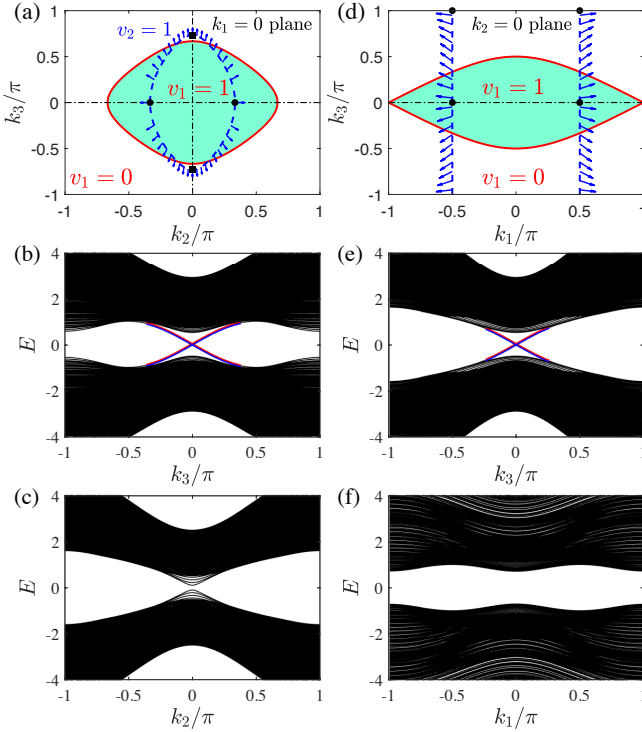


Figure 5. (color online). (a) Nested BISs for Hamiltonian $H^{(D)}(\mathbf{k})$ of Eq. (24) with an asymmetric parameter γ , where $\gamma = 0.3$ has been set. $S_1^{m=2}$, $S_2^{m=1}$, and the vector (h_2, h_3) are indicated by red solid loop, blue dashed loop and blue arrow respectively. 2-BISs $S_2^{m=2,a}$ and $S_2^{m=2,b}$ of $H_2^{(D)}(\mathbf{k}_{1,\parallel})$ are indicated by black dots and squares, respectively. (b) and (c) Energy spectra corresponding to (a) with PBC taken only in r_3 - and r_2 -directions, respectively. (d) The nested-BIS for Hamiltonian $H^{(D)}(\mathbf{k})$ with the decomposition of Eq. (38). (e) and (f) Energy spectra corresponding to (b) with PBC taken only in r_3 - and r_1 -directions, respectively. In all panels, $m_1 = -1.5$ and $m_2 = -0.5$ are set.

2-BISs for $H_2^{(D)}(\mathbf{k}_{1,\parallel})$ as

$$S_2^{m=2,a} : M_2 = h_3 = 0, \quad S_2^{m=2,b} : M_2 = h_2 = 0.$$

As shown in Fig. 5(a), $S_2^{m=2,a}$ falls within the region with a nonzero v_1 , and it holds a nonzero topological invariant

$$v_2 = \frac{1}{2} \sum_{S_2^{m=2,a}} \text{Sgn}[\frac{\partial M_2}{\partial k_2} h_2] = 1$$

for the parameters we choose [34, 42]. Note that by definition, this v_2 corresponds not to the winding of (h_2, h_3) shown in Fig. 5(a), but to the winding of (h_2, M_2) at $k_3 = 0$, with k_2 varying from 0 to 2π . Nevertheless, these two winding properties are equivalent as they both reflect the 2D Chern topology of $H_2^{(D)}(\mathbf{k}_{1,\parallel})$. Furthermore, a nonzero v_2 describes a nontrivial 1D topology along k_2 -direction at $k_3 = 0$, corresponding to a pair of chiral edge states of $H_2^{(D)}(\mathbf{k}_{1,\parallel})$ when OBC is taken along

r_2 -direction. Due to the nested relation between $S_2^{m=2,a}$ and $S_2^{m=1}$, such topological properties can be captured by the surface states of $H_1^{(D)}(\mathbf{k}_{1,\parallel})$ and manifests as chiral-like hinge states in Fig. 5(b).

Similarly, a topological invariant defined for $S_2^{m=2,b}$ characterizes topological properties along k_3 (r_3) direction. However, $S_2^{m=2,b}$ falls outside the nonzero region of v_1 enclosed by $S_1^{m=2}$, meaning that its topological properties (if any) cannot be captured by the surface states. Therefore the overall system shows a trivial 2nd-order topology when OBC is taken along r_2 -direction, in consistent with the absence of chiral-like hinge states in Fig. 5(c). Note that in both Figs. 5(b) and (c) we have also taken OBC along r_1 -direction, and PBC along the third direction, so to illustrate only the 2nd-order topology associated to the two OBC directions in each case.

2. Asymmetric properties between k_1 and k_3

As a matter of fact, the asymmetric behavior of hinge states and BISs can also be seen in the original Hamiltonian of Eq. (24), where \mathcal{C}_4 rotation symmetry holds only in k_2 - k_3 plane, but not in the other two planes involving k_1 . To see this, we rewrite the Hamiltonian as

$$\begin{aligned} H^{(D)}(\mathbf{k}) &= H_1^{(D)}(\mathbf{k}) + H_2^{(D)}(k_1, k_3), \\ H_1^{(D)}(\mathbf{k}) &= \widetilde{M}_1(\mathbf{k})(\sigma_x \tau_0 + \sigma_z \tau_x)/\sqrt{2} + h_2(\mathbf{k})\sigma_z \tau_y \\ H_2^{(D)}(k_1, k_3) &= \widetilde{M}_2(k_1, k_3)(\sigma_x \tau_0 - \sigma_z \tau_x)/\sqrt{2}, \\ &\quad + h_1(k_1)\sigma_y \tau_0 + h_3(k_3)\sigma_z \tau_z, \end{aligned} \quad (38)$$

where $\widetilde{M}_1 = (M_1 + M_2)/\sqrt{2} = (m_1 + m_2 + 5 - \cos k_1 - 2 \cos k_2 - 2 \cos k_3)/\sqrt{2}$, $\widetilde{M}_2 = (M_1 - M_2)/\sqrt{2} = (m_1 - m_2 + 1 - \cos k_1)/\sqrt{2}$, and $h_i = \sin k_i$ with $i = 1, 2, 3$ as for Eq. (24). These terms also anti-communicate with each others, and now it is k_2 that appears only in $H_1^{(D)}(\mathbf{k})$. Therefore with this alternative expression of $H^{(D)}(\mathbf{k})$, we can apply the nested-BIS method to analysis how the topological properties of $H_2^{(D)}(k_1, k_3)$ are captured by the surface states under OBC along r_2 -direction.

To proceed further, we first define a 2-BIS $S_1^{m=2} : H_1^{(D)} = 0$ of $H_1^{(D)}$, and a 1-BIS $S_2^{m=1}$ of $H_2^{(D)}$. Similar to the previous asymmetric example, here $S_2^{m=1}$ crosses $S_1^{m=2}$ as it is separated into two lines paralleling to k_3 . Therefore we need to further define a 2-BIS for $H_2^{(D)}$ as $S_2^{m=2,a} : \widetilde{M}_2 = h_3 = 0$, which are two pairs of points at $k_3 = 0$ or $k_3 = \pi$, as shown in Fig. 5(d). For each pair of the 2-BIS with the same k_3 , a topological invariant can be obtained as

$$v_2(k_3 = 0/\pi) = \frac{1}{2} \sum_{S_2^{m=2,a}, k_3=0/\pi} \text{Sgn}[\frac{\partial \widetilde{M}_2}{\partial k_1} h_1] = 1,$$

meaning that a 2D system described by $H_2^{(D)}(k_1, k_3)$

holds counterpropagating edge states [52–54] at momentum $k_3 = 0$ and π when r_1 -direction takes OBC. However, only one pair of $S_2^{m=2,a}$ (with $k = 0$) falls within the region with nonzero v_1 , and its nontrivial topology is captured by the surface states of $H_1^{(D)}$, manifested as a single pair of chiral-like hinge states (on each surface) under OBCs along r_1 - and r_2 -directions, as shown in Fig. 5(e). In contrast, there is no hinge state when r_2 - and r_3 -directions take OBCs, as shown in Fig. 5(f). Compared with the results in Fig. 2(a) and (b) for the same system, we can see that this 3D second-order topological phase holds asymmetric topological properties in 2D planes lacking a C_4 rotation symmetry, i.e., the topological boundary states may exist only along certain hinges of these planes.

B. Effects of non-Clifford operators

Finally, we extend the nested-BIS method beyond the Clifford algebra by introducing extra non-anticommuting terms. In general, non-Clifford operators can be obtained as the product of several operators from the Clifford algebra. For the HOTPs we consider, coefficients of these non-Clifford operators are further restricted by the symmetry class of the system. Explicitly, we take the Hamiltonian of Eq. (24) as an example, and introduce non-Clifford terms as products of the operators of the two mass terms $M_{1,2}$, and one of the rest three terms $h_{1,2,3}$, given by

$$\begin{aligned} g_1 \bar{\Gamma}^1 &\equiv i g_1 (\sigma_x \tau_0) (\sigma_z \tau_x) (\sigma_y \tau_0) = g_1 \sigma_0 \tau_x, \\ g_2 \bar{\Gamma}^2 &\equiv i g_2 (\sigma_x \tau_0) (\sigma_z \tau_x) (\sigma_z \tau_y) = -g_2 \sigma_x \tau_z, \\ g_3 \bar{\Gamma}^3 &\equiv i g_3 (\sigma_x \tau_0) (\sigma_z \tau_x) (\sigma_z \tau_z) = g_3 \sigma_x \tau_y, \end{aligned}$$

with $g_{1,2,3}$ some \mathbf{k} -independent parameters. Obviously, these terms keep the particle-hole symmetry $\mathcal{C} \bar{\Gamma}^{1,2,3} \mathcal{C}^{-1} = -\bar{\Gamma}^{1,2,3}$ with $\mathcal{C} = \sigma_z \tau_z \mathcal{K}$, hence the system remains in the D class with $Z \times Z$ topology. On the other hand, certain spatial symmetries will be broken with nonzero $g_{1,2,3}$, leading to asymmetric boundary states between different hinges of the 3D system. Specifically, the original Hamiltonian with $g_{1,2,3} = 0$ satisfies the C_4 rotation symmetry of Eq. (36), and three chiral-mirror symmetries associated with the three directions,

$$\begin{aligned} -H^{(D)}(k_1, k_2, k_3) &= \sigma_y \tau_0 H^{(D)}(-k_1, k_2, k_3) \sigma_y \tau_0 \\ &= \sigma_z \tau_y H^{(D)}(k_1, -k_2, k_3) \sigma_z \tau_y \\ &= \sigma_z \tau_z H^{(D)}(k_1, k_2, -k_3) \sigma_z \tau_z. \end{aligned} \quad (39)$$

Consequently, topological boundary states must emerge along different hinges related by these symmetries. A nonzero g_1 breaks the chiral-mirror symmetry along r_1 -direction and induces asymmetric behavior between (100) and $(\bar{1}00)$ surfaces. Thus it is referred as a longitudinal non-Clifford term henceforth. In contrast, the other two terms are referred as mixed non-Clifford terms, as a

nonzero g_2 (g_3) breaks not only the chiral-mirror symmetry along r_2 -(r_3)-direction, and also the C_4 rotation symmetry. These two mixed non-Clifford terms can be mapped to each other through the C_4 rotation operation, $C_4 \bar{\Gamma}^2 C_4^{-1} = -\bar{\Gamma}^3$ [55], and we shall discuss only the first one in details. Further, we assume these terms are relatively weak compared with other parameters, otherwise the system may be driven to other 1st-order topological phases, e.g., a topological semimetal [56, 57] or a weak topological insulator [58–60], as discussed in Appendix C with more details.

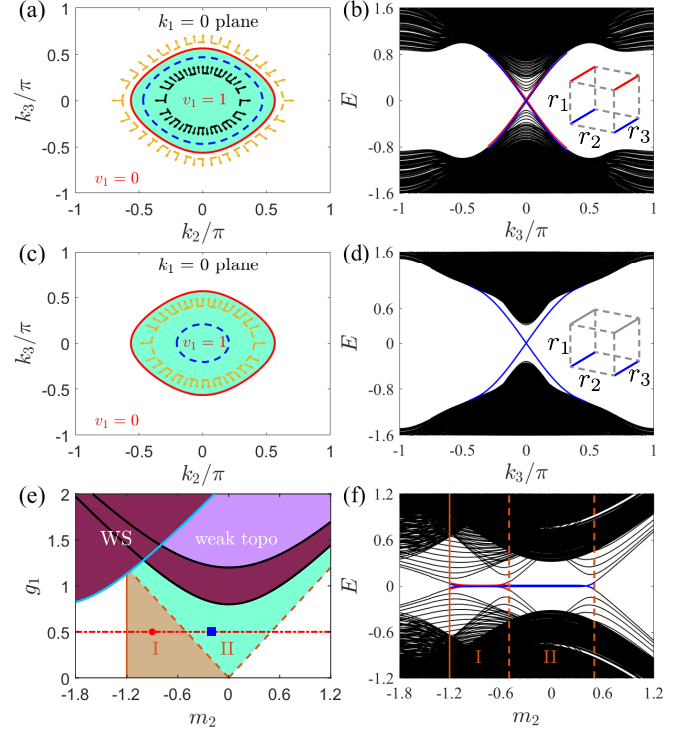


Figure 6. (color online) (a) Nested BISs for the Hamiltonian $H^{(D)}(\mathbf{k})$ with the longitudinal non-Clifford term $g_1 \sigma_0 \tau_x$ of Eq. (40), with $m_1 = -1.2$, $g_1 = 0.5$ and $m_2 = -0.9$. $S_1^{m=2}$, $S_2^{m=1}$, and the vector (h_2, h_3) are indicated by red solid loop, blue dash loop and blue arrows respectively, and the extra BIS $S_{+,2}^{m=1}$ ($S_{-,2}^{m=1}$) is marked by black (orange) dash loops. Arrows attached to BISs indicate the vector (h_2, h_3) . (b) Energy spectra corresponding to (a). Red and blue lines in the inset indicate the emergence of hinge states on (100) and $(\bar{1}00)$ surfaces, respectively. (c) and (d) The same results as in (a) and (b), but with $m_2 = -0.2$. $S_{+,2}^{m=1}$ and hinge states on (100) surface are seen to disappear. (e) A phase diagram for Hamiltonian $H^{(D)}(\mathbf{k})$ of Eq. (40) with $m_1 = -1.2$. “WS” and “weak topo” represents Weyl semimetallic and weak topological phases, which are discussed in Appendix. Red dot (blue square) corresponds to the parameters used in (a) and (b) [(c) and (d)]. (f) Energy spectrum at $k_3 = 0$ along the red horizontal line ($g_1 = 0.5$) in (e), where r_1 - and r_2 -directions take OBCs.

1. HOTPs with the longitudinal non-Clifford term

First, we add the longitudinal non-Clifford term $g_1\sigma_0\tau_x$ to the Hamiltonian of Eq. (24), and rewrite it as:

$$\begin{aligned} H^{(D)}(\mathbf{k}) &= H_1^{(D)}(\mathbf{k}) + H_2^{(D)}(\mathbf{k}_{1,\parallel}), \\ H_1^{(D)}(\mathbf{k}) &= M_1(\mathbf{k})\sigma_x\tau_0 + h_1(\mathbf{k})\sigma_y\tau_0, \\ H_2^{(D)}(\mathbf{k}_{1,\parallel}) &= M_2(\mathbf{k}_{1,\parallel})\sigma_z\tau_x + g_1\sigma_0\tau_x \\ &\quad + h_2(\mathbf{k}_{1,\parallel})\sigma_z\tau_y + h_3(\mathbf{k}_{1,\parallel})\sigma_z\tau_z. \end{aligned} \quad (40)$$

In this decomposition, surface states of $H_1^{(D)}(\mathbf{k})$ along r_1 -direction appear when the first topological invariant $v_1 \neq 0$ [defined in Eq. (25)]. To see how the topological properties of $H_2^{(D)}(\mathbf{k}_{1,\parallel})$ are captured by these surface states, we obtain effective 2D Hamiltonians for surface states through the projection of $P_{1,\pm}$,

$$\begin{aligned} H_{\text{eff},\pm}^{(D)} &= P_{1,\pm} H_2^{(D)} P_{1,\pm} \\ &= P_{1,\pm} [(M_2 \pm g_1)\sigma_z\tau_x + h_2\sigma_z\tau_y + h_3\sigma_z\tau_z] P_{1,\pm}, \\ P_{1,\pm} &= [1 \pm i(\sigma_y\tau_0)(\sigma_x\tau_0)]/2 = (1 \pm \sigma_z\tau_0)/2, \end{aligned} \quad (41)$$

whose topology can be determined by their 1-BIS $S_{\pm,2}^{m=1}$: $M_2 \pm g_1 = 0$. Obviously the effective Hamiltonians for surface states on the (100) and ($\bar{1}00$) surfaces are different in the presence of the longitudinal non-Clifford term, which breaks the chiral-mirror symmetry $\sigma_y\tau_0 H^{(D)}(-k_1, k_2, k_3)\sigma_y\tau_0 = -H^{(D)}(k_1, k_2, k_3)$. As a consequence, asymmetric behavior for these two surfaces are expected for the topological boundary states.

Interestingly, although the 1st-order topology of $H_{\text{eff},\pm}^{(D)}$ is associated with their BISs $S_{\pm,2}^{m=1}$, it is the nested relation associated with $S_2^{m=1}$ for $H_2^{(D)}$ that determines whether their topological properties are inherited by the surface states of $H_1^{(D)}$, as shown by two typical examples in Figs. 6(a) to (d). In Fig. 6(a), both $H_{\text{eff},\pm}^{(D)}$ are topologically nontrivial, yet their BISs $S_{\pm,2}^{m=1}$ (black and yellow dash loops) falls outside and inside the nontrivial region of v_1 respectively. Nevertheless, $S_2^{m=1}$ falls within the nontrivial region of v_1 , and chiral-like hinge states emerge on both (100) and ($\bar{1}00$) surfaces, as shown by the spectrum with OBCs along r_1 - and r_2 -directions [Fig. 6(b)]. In Fig. 6(c), $H_{\text{eff},+}^{(D)}$ becomes topologically trivial and its BIS $S_{+,2}^{m=1}$ disappears. Consistently, chiral-like hinge states exist only on ($\bar{1}00$) surfaces, as shown in Fig. 6(d) with the same boundary conditions. We note results with OBCs along r_1 - and r_3 -directions are identical, as the system possesses the \mathcal{C}_4 rotation symmetry in k_2 - k_3 plane.

In Fig. 6(e), we display the phase diagram in g_1 - m_2 parameter space with constant value of m_1 . The corresponding energy spectrum at $k_3 = 0$, namely the crossing point of the chiral-like hinge states, is displayed in Fig. 6(f) for $g_1 = 0.5$. The two topologically nontrivial phases can thus be identified by the number of zero-energy states in the spectrum, denoted as phases I and

II in these two panels. The phase boundaries can also be classified into two types. The first one is marked by the orange solid line at $m_2 = m_1 = -1.2$, which is independent from g_1 . It stands for the case where $S_2^{m=1}$, the BIS for $H_2^{(D)}$, coincides with $S_1^{m=2}$, the BIS for $H_1^{(D)}$ separating trivial and nontrivial regions of v_1 . For $m_2 < -1.2$, $S_2^{m=1}$ falls outside the nontrivial region of v_1 and the 2nd-order topology becomes trivial. On the other hand, the other type of phase boundaries are marked by the orange dash lines, where one of $S_{\pm,2}^{m=1}$ vanishes, and the corresponding surface Hamiltonian $H_{\text{eff},\pm}^{(D)}$ becomes trivial. Notably, in our system, $S_2^{m=1}$ will vanish before $S_{-,2}^{m=1}$ when increasing m_2 . However, such a transition does not involve any crossing of different BISs, and hence shall not change the inheriting relation of topology. To conclude our results, nontrivial topology of $H_{\text{eff},\pm}^{(D)}$ characterized by their own BISs $S_{\pm,2}^{m=1}$ are inherited by the surface states of $H_1^{(D)}$, as long as the BIS $S_2^{m=1}$ for $H_2^{(D)}$ falls, or even vanishes, within the nontrivial region of v_1 .

Finally, we note that increasing g_1 can drive the system into a topological semimetal [56, 57] or a weak topological insulator [58–60], as indicated in the phase diagram of Fig. 6(e). In such cases, surface states protected by 2D 1st-order topology will appear, instead of the higher-order hinge states characterized by our current method of nested BISs (see Appendix C for more details).

2. HOTPs with a mixed non-Clifford term

Next we consider the effect of adding $-g_2\sigma_x\tau_z$, one of the two mixed non-Clifford terms, to the Hamiltonian of Eq. (24). We find that in this case, it is more convenient to use the decomposition in Eq. (38) and rewrite the Hamiltonian as

$$\begin{aligned} H^{(D)}(\mathbf{k}) &= H_1^{(D)}(\mathbf{k}) + H_2^{(D)}(k_1, k_3), \\ H_1^{(D)}(\mathbf{k}) &= \widetilde{M}_1(\mathbf{k})(\sigma_x\tau_0 + \sigma_z\tau_x)/\sqrt{2} + h_2(\mathbf{k})\sigma_z\tau_y, \\ H_2^{(D)}(k_1, k_3) &= \widetilde{M}_2(k_1, k_3)(\sigma_x\tau_0 - \sigma_z\tau_x)/\sqrt{2} - g_2\sigma_x\tau_z \\ &\quad + h_1(k_1, k_3)\sigma_y\tau_0 + h_3(k_1, k_3)\sigma_z\tau_z, \end{aligned} \quad (42)$$

where $H_1^{(D)}(\mathbf{k})$ now determines the surface states along r_2 -directions, i.e. on (010) and ($0\bar{1}0$) surfaces. Regarding the (anti-)commuting relations between different components, this decomposition takes a similar form as the previous case with the longitudinal non-Clifford term, and hence the conclusion is also expected to apply here. However, due to the absence of a \mathcal{C}_4 rotation symmetry in k_1 - k_3 plane, the BISs may cross each other and induce asymmetric behaviors between hinge states along r_1 and r_3 directions, as discussed in Sec. VIA. To see this, we first write down the effective Hamiltonians for the surface states on (010) and ($0\bar{1}0$) surfaces through the cor-

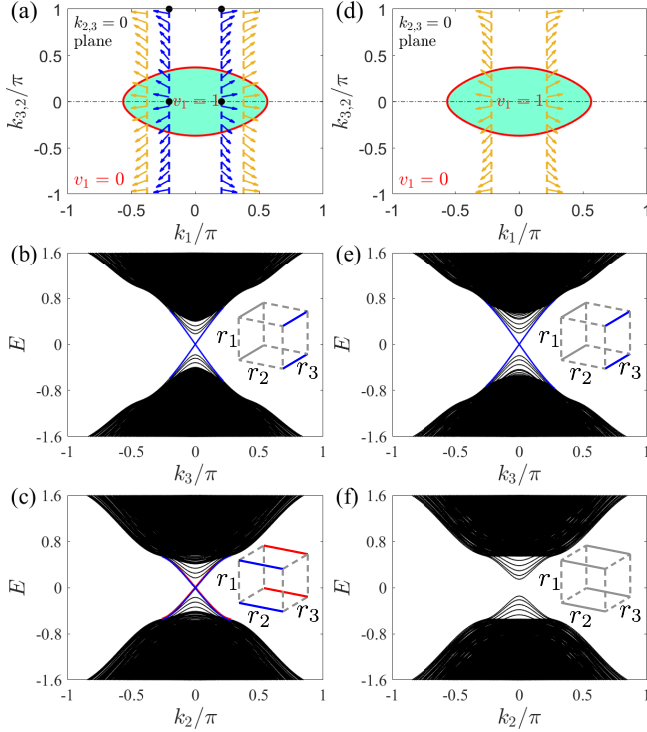


Figure 7. (color online). (a) Nested BIS for Hamiltonian $H^{(D)}(\mathbf{k})$ with the mixed non-Clifford term $-g_2\sigma_x\tau_z$, with $m_+ \equiv m_1 + m_2 = 1.2$, $m_- \equiv m_1 - m_2 = -0.2$ and $g_2 = 0.3$. $S_1^{m=2}$ and $S_2^{m=1}$ are indicated by red solid loop and blue dash lines respectively. Black dots mark the 2-BIS $S_2^{m=2}$ of $H_2^{(D)}$. These BISs are identical for the two decomposition of Eqs. (42) and (44) upon a transformation $k_2 \leftrightarrow k_3$, and hence we put them in the same figure for convenience. Yellow dash lines indicate $S_{\pm,2}^{m=1}$ in k_1 - k_3 plane for the effective Hamiltonian in Eqs. (43), with $S_{\pm,2}^{m=1}$ vanishes for the chosen parameters. For Eqs. (45), Both $S_{\pm,2}^{m=1}$ in k_1 - k_2 plane are identical to $S_2^{m=1}$ for $H_2^{(D)}$ in Eqs. (44). Yellow and blue arrows represent the vectors (h_1, h_3) and (h_1, h_2) along their corresponding BISs respectively. (b) and (c) Energy spectra corresponding to (a), with OBCs along r_1/r_2 - and r_1/r_3 - directions respectively. Red and blue lines in the insets indicate the hinge states on (010) and (0 $\bar{1}$ 0) [(001) and (00 $\bar{1}$)] surface for (b) [(c)]. (d) to (f) The same results as in (a) to (c) but with $m_- = 0.2$. The BIS $S_2^{m=1}$ vanishes in (d). Correspondingly, no hinge state exist in (f) with OBCs along r_1/r_3 -directions.

responding projection operators:

$$\begin{aligned}
 H_{\text{eff},\pm}^{(D)} &= P_{2,\pm} H_2^{(D)} P_{2,\pm} \\
 &= P_{2,\pm} [(\tilde{M}_2 \pm g_2)(\sigma_x\tau_0 - \sigma_z\tau_x)/\sqrt{2} \\
 &\quad + h_1\sigma_y\tau_0 + h_3\sigma_z\tau_z] P_{2,\pm}, \\
 P_{2,\pm} &= [1 \pm i(\sigma_z\tau_y)(\sigma_x\tau_0 + \sigma_z\tau_x)/\sqrt{2}]/2 \\
 &= [1 \pm (\sigma_0\tau_z - \sigma_y\tau_y)/\sqrt{2}]/2.
 \end{aligned} \tag{43}$$

Following previous discussion, we need to consider a BIS for each of $H_{\text{eff},\pm}^{(D)}$, defined as

$$S_{\pm,1}^{m=2} : \tilde{M}_2 \pm g_2 = 0,$$

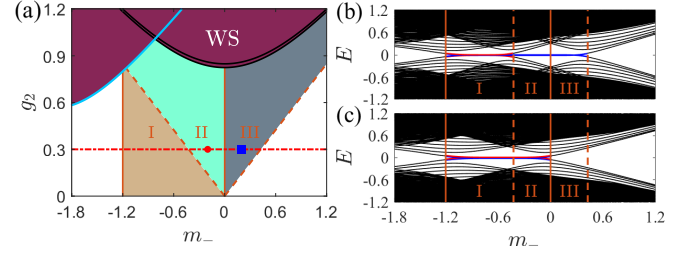


Figure 8. (color online). (a) A phase diagram for Hamiltonian $H^{(D)}(\mathbf{k})$ of Eq. (42), with the mixed non-Clifford term $-g_2\sigma_x\tau_z$ and $m_+ = -1.2$. Parameters used in Fig. 7(a) to (c) [(e) to (f)] is marked with a red dot (blue square). (b) Energy spectrum at $k_3 = 0$ along the red horizontal lines ($g_2 = 0.3$) in (a), with OBCs taken for r_1 - and r_2 -directions. (c) Energy spectrum at $k_2 = 0$ along the red horizontal lines in (a), with OBCs taken for r_1 - and r_3 -directions. For $m_- < -1/2$, $S_1^{m=2}$ falls outside $S_1^{m=2}$ for both cases, and the zero-energy states disappear in both (b) and (c). At the two orange dash lines, one of $S_{\pm,2}^{m=1}$ defined for $H_{\text{eff},\pm}^{(D)}$ in Eq. (43) vanishes, and a pair of zero-energy states disappears in (b) when m_- exceeds each dash line. When $m_- > 0$, $S_{\pm,2}^{m=2}$ (identical to $S_2^{m=2}$) for $H_{\text{eff},\pm}^{(D)}$ in Eq. (45) vanishes, meaning these effective Hamiltonians for (001) and (00 $\bar{1}$) become topologically trivial, and zero-energy states disappear in (c).

which characterize topological properties of the effective Hamiltonians; and another one for $H_2^{(D)}$, which determines whether these topological properties are inherited by surface states along r_2 -direction and manifested as chiral-like hinge states. Similarly to the cases in Sec. VIA, the 1-BIS of $H_2^{(D)}$ crosses the 2-BIS

$$S_1^{m=2} : \tilde{M}_1 = h_2 = 0$$

defined for $H_1^{(D)}$, as shown in Fig. 7(a) and (d). Therefore to apply the nested-BIS method, we shall follow our discussion in Sec. VIA and consider a 2-BIS of $H_2^{(D)}$,

$$S_2^{m=2} : \tilde{M}_2 = h_3 = 0.$$

We can see in Figs. 7(a) and (d) that $S_2^{m=2}$ falls and vanishes within the nontrivial regime of ν_1 respectively, so that the nontrivial topology of $H_{\text{eff},-}^{(D)}$ is manifested as chiral-like hinge states on (0 $\bar{1}$ 0) surface as shown in Figs. 7(b) and (e). For the parameters chosen in these figures, $H_{\text{eff},+}^{(D)}$ is topologically trivial as $S_{+,1}^{m=2}$ disappears, and no hinge state emerges on (010) surface. The physics behind this asymmetric behavior is straightforward: a nonzero g_2 breaks the chiral-mirror symmetry along k_2 -direction [see Eq. (39)], and may induce different topological properties on (010) and (0 $\bar{1}$ 0) surfaces.

In contrast, the other two chiral-mirror symmetries along k_1 - and k_3 -directions are not violated by g_2 , and symmetric behaviors are expected for these two directions. In Figs. 7(b) and (e) we already see that the hinge states are symmetric between (100) and (1 $\bar{0}$ 0) sur-

faces. To analyze hinge states on (001) and (00 $\bar{1}$) surfaces, we consider a different decomposition and rewrite the Hamiltonian as

$$\begin{aligned} H^{(D)}(\mathbf{k}) &= H_1^{(D)}(\mathbf{k}) + H_2^{(D)}(k_1, k_2), \\ H_1^{(D)}(\mathbf{k}) &= \widetilde{M}_1(\mathbf{k})(\sigma_x\tau_0 + \sigma_z\tau_x)/\sqrt{2} + h_3(\mathbf{k})\sigma_z\tau_z, \\ H_2^{(D)}(k_1, k_2) &= \widetilde{M}_2(k_1, k_2)(\sigma_x\tau_0 - \sigma_z\tau_x)/\sqrt{2} - g_2\sigma_x\tau_z \\ &\quad + h_1(k_1, k_2)\sigma_y\tau_0 + h_2(k_1, k_2)\sigma_z\tau_y, \end{aligned} \quad (44)$$

so that k_3 is contained only in $H_1^{(D)}(\mathbf{k})$. Next, the effective Hamiltonians for surface states on (001) and (00 $\bar{1}$) surfaces are given by projecting $H_2^{(D)}$ on these two surfaces,

$$\begin{aligned} H_{\text{eff},\pm}^{(D)} &= P_{3,\pm} H_2^{(D)} P_{3,\pm} \\ &= P_{3,\pm} [\widetilde{M}_2(\sigma_x\tau_0 - \sigma_z\tau_x)/\sqrt{2} \\ &\quad + h_1\sigma_y\tau_0 + h_2\sigma_z\tau_y] P_{3,\pm}, \\ P_{3,\pm} &= [1 \pm i(\sigma_z\tau_z)(\sigma_x\tau_0 + \sigma_z\tau_x)/\sqrt{2}]/2 \\ &= [1 \mp (\sigma_y\tau_z + \sigma_0\tau_y)/\sqrt{2}]/2. \end{aligned} \quad (45)$$

Comparing Eqs. (44) and (45) with Eqs. (42) and (43), we can see that the two BISs defined for the latter case,

$$S_1^{m=2} : \widetilde{M}_1 = h_3 = 0, \quad S_2^{m=2} : \widetilde{M}_2 = h_2 = 0,$$

are identical to those of the previous case upon exchanging two momentum components, $k_2 \leftrightarrow k_3$. However, now that g_2 does not enter the two effective Hamiltonians in Eq. (43), therefore their BISs become the same as $S_2^{m=2}$, and appearance of chiral-like hinge states on (001) and (00 $\bar{1}$) surfaces are not affected by this mixed non-Clifford term. This prediction consists with our numerical results for OBCs along r_1 and r_3 directions. In Fig. 7(c), a pair of chiral-like hinge states is seen on each of (001) and (00 $\bar{1}$) surfaces, as $S_2^{m=2}$ falls within the nontrivial region of v_1 in In Fig. 7(a). On the other hand, Fig. 7(f) represents a topologically trivial case without any hinge state, as $S_2^{m=2}$ vanishes in Fig. 7(d), indicating trivial topology of $H_{\text{eff},\pm}^{(D)}$ in Eq. (45). Compared with Figs. 7(b) and (e), it is also seen that hinge states behave differently under OBCs along r_2 - and r_3 -directions, as a consequence of breaking the \mathcal{C}_4 rotation symmetry by a nonzero g_2 .

Combining these results, we obtain a phase diagram by analyzing the BISs of the system, as shown in Fig. 8(a). In phase I, chiral-like hinge states emerge on both surfaces along either r_2 - or r_3 directions, analogous to phase I for the case with the longitudinal non-Clifford term. Phases II and III are two topological phases where hinge states emerge asymmetrically between these two directions, as shown by the two examples in Fig. 7. To give a clear view of the topological phase transitions, we display the energy spectrum at $k_3 = 0$ under OBCs along r_1 - and r_2 - directions in Fig. 8(b), and that at $k_2 = 0$ under OBCs along r_1 - and r_3 - directions in Fig. 8(b). The appearance and disappearance of topological hinge states

are seen to match the topological transition predicted by BISs very well. Also when g_2 becomes larger, the system will enter semimetallic phases [56, 57] as shown in Fig. 8(a), which can support surface states protected by 2D 1st-order topology (see Appendix C for more details).

VII. DISCUSSION

The concept of HOTPs has broadly extended our knowledge of topological phases of matter, as many systems previously considered trivial according to the standard AZ symmetry classification have been found to support higher-order topological states at boundaries of boundaries. In this work, we exhaustively investigate the emergence of HOTPs based on the AZ classification, and propose a universal scheme to construct HOTPs in each AZ class with the nested-BIS method. An n th-order topological phase constructed in this way is topologically characterized by the geometric (nested) relation between n BISs of the system, defined as where certain pseudospin components vanish in the BZ; and by Z^n , $2Z^n$, or $Z^{n-1} \times Z_2$ topological invariants, depending on which symmetry class the system belongs to. These results are unveiled with both general minimal continuous Hamiltonians, and several example lattice models with the continuous Hamiltonians taken as effective Hamiltonians at some high-symmetric points. While the lattice examples considered here are either 2D or 3D, our scheme can apply to much more general scenarios without restriction of spatial dimension or order of topology. To generalize our discussion, we further consider cases with crossed BISs or/and non-Clifford operator, where higher-order boundary states become asymmetric due to the breaking of certain spatial symmetries by extra modulations to the Hamiltonian, allowing us to tune the configuration of higher-order boundary states in a flexible way.

In addition to offering a theoretical tool for investigating HOTPs from lower-order topology, our scheme are also useful for engineering HOTPs and probing their topological properties in various experiments. The explicit construction using our scheme involves proper design of different pseudospin component, thus it is most applicable for quantum simulation with single or a few qubits, with their parameters serving as crystal momentum to form a synthetic BZ [43, 61–65]. The BISs and corresponding topological invariants can be probed through measuring time-averaged pseudospin texture over long-time dynamics [34, 41, 42, 51, 66–70], which has already been realized in several experimental platforms, such as superconducting qubits [71] and ultracold atoms [72, 73]. Furthermore, we note that while the current study focuses only on gapped HOTPs, we also expect our method, with proper modifications, to be applicable in the study of higher-order semimetallic phases [74–79].

ACKNOWLEDGMENTS

This work is supported by the National Key R&D Program of China (Grant No. 2018YFA0307500), the NSFC (Grants No. 12104519, No. 11874433, No. 12135018), and the Guangdong Basic and Applied Basic Research Foundation (2020A1515110773).

Appendix A: Classification of general higher-order topological phases

In the main text, we have provided a table of symmetry classification for second-order topological phases. In this appendix we discuss the behaviour when the order of topology increases and give a general classification of the HOTPs phases based on the nested-BIS method.

As described in Sec III B of the main text, a d D Hamiltonian $H^{(d,n)}(\mathbf{k})$ supporting n -order HOTPs with Z^n topological invariant contains $J = d + n$ anti-commuting terms, including several purely real matrices coupled to crystal momentum. A corresponding anti-unitary symmetry operator \hat{A} is given by the product of these real matrices and the complex conjugate operator \mathcal{K} , such as in (12) and (18) of the main text. In addition, if this Hamiltonian supports chiral symmetry with the symmetry operator \hat{S} , another anti-unitary symmetry operator can be obtained as $\hat{A}\hat{S}$, which is also a product of real matrices since \hat{S} is purely real in our construction. Therefore all anti-unitary symmetry operators in our models are given by the product of the complex conjugate operator \mathcal{K} and several purely real matrices, which may be coupled only to crystal momentum in the Hamiltonian.

Without loss of generality, we assume $H^{(d,n)}(\mathbf{k})$ holds an anti-unitary symmetry

$$\hat{A}H^{(d,n)}(\mathbf{k})\hat{A}^{-1} = (-1)^a H^{(d,n)}(-\mathbf{k}) \quad (\text{A1})$$

with $\hat{A}^2 = (-1)^{a(a-1)/2}$, where \hat{A} is given by the product of a purely real matrices and \mathcal{K} . Next, we choose a momentum component of the Hamiltonian and transform it into a mass term, i.e. $k_\beta \Gamma_{(2p+1)}^{2\alpha+1} \rightarrow m \Gamma_{(2p+1)}^{2\alpha+1}$. In this way we obtain a $(d-1)$ D Hamiltonian $H^{(d-1,n+1)}(\mathbf{k})$ supporting $(n+1)$ -order HOTPs. Obviously, this mass term breaks the above anti-unitary symmetry, $\hat{A}m\Gamma_{(2p+1)}^{2\alpha+1}\hat{A}^{-1} \neq (-1)^a m\Gamma_{(2p+1)}^{2\alpha+1}$. Instead, we can define another anti-unitary symmetry $\hat{A}' = \Gamma_{(2p+1)}^{2\alpha+1}\hat{A}$, equivalent to removing $\Gamma_{(2p+1)}^{2\alpha+1}$ from \hat{A} . That is, the operator \hat{A}' is given by of $(a-1)$ purely real matrices, satisfying

$$\hat{A}'m\Gamma_{(2p+1)}^{2\alpha+1}\hat{A}'^{-1} = (-1)^{a-1}m\Gamma_{(2p+1)}^{2\alpha+1}.$$

Furthermore, the rest of the Hamiltonian does not contain $\Gamma_{(2p+1)}^{2\alpha+1}$ and hence also satisfies a condition similar to Eq. (A1), leading to an anti-unitary symmetry for the

whole system, described by

$$\hat{A}'H^{(d-1,n+1)}(\mathbf{k})\hat{A}'^{-1} = (-1)^{a-1}H^{(d-1,n+1)}(-\mathbf{k}). \quad (\text{A2})$$

Therefore, if \hat{A} describes a particle-hole symmetry \mathcal{C} with $\hat{A}^2 = \pm 1$ (time-reversal symmetry \mathcal{T} with $\hat{A}^2 = \pm 1$) for $H^{(d,n)}(\mathbf{k})$, \hat{A}' describes a time-reversal symmetry \mathcal{T} with $[\hat{A}']^2 = \pm 1$ (particle-hole symmetry \mathcal{C} with $[\hat{A}']^2 = \mp 1$) for $H^{(d-1,n+1)}(\mathbf{k})$.

To conclude, compared with $H^{(d,n)}(\mathbf{k})$ with Z^n topological invariant, $H^{(d-1,n+1)}(\mathbf{k})$ describes a system with one order higher of topology, and is shifted one column to the left (as the spatial dimension is reduced by 1) and up two rows (due to the changing of symmetry condition) in the symmetry classification table. Finally, HOTPs with Z_2 topological properties can be derived from a parent Hamiltonian indexed by Z^n , as discussed in Sec V of the main text. Therefore they also obey the same shifting rule as for the Z^n systems. Therefore a general symmetry classification table is obtained for arbitrary orders of topology in arbitrary spatial dimensions, as shown in table A1.

Appendix B: Properties of the Z_2 invariants

In Sec V of the main text, we have discussed the HOTP with Z_2 topological invariant, where the interpolation of Eq. (35) have been introduced to define the topological properties of H_2 in Eq. (34). To reveal the Z_2 properties of topological invariants v_2 , we provide another interpolation:

$$\begin{aligned} \tilde{H}_2^{(D,1)}(k_2, \theta) = & \tilde{M}_2(k_2, \theta)\sigma_z\tau_x + \tilde{h}_2(k_2, \theta)\sigma_z\tau_y \\ & + \tilde{f}_1(k_2, \theta)\sigma_z\tau_z. \end{aligned} \quad (\text{B1})$$

Compared with Eq. (35), here we keep the same form of

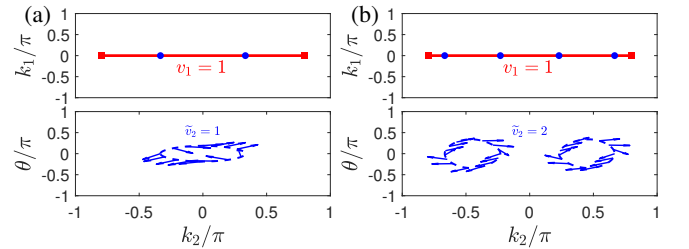


Figure B1. (color online). Nested BISs for Hamiltonian $H^{(D,1)}(\mathbf{k})$ of Eq. (34) of main text and the vector $(\tilde{h}_2, \tilde{f}_1)$ along the BIS $\tilde{S}_2^{m=1}$ for interpolation of Eq. (B1), where $b = 3$ is set. Here $S_1^{m=2}$ and $S_2^{m=1}$ are indicated by red squares and blue dots, respectively. In all panels $m_1 = -1.8$, $m_2 = -0.5$, and $\lambda_2 = 3$ have been set, and $\lambda_1 = 0$ ($\lambda_1 = -2$) for (a) [(b)].

\tilde{M}_2 , but introduce a different $\tilde{f}_1(k_2, \theta)$ and a θ -dependant

Table A1. Classification of n th-order HOTPs based on the nested-BIS method. The continuous Hamiltonians for topological phases characterized by n Z -invariants are provided with $H^{(I)}$ in Eq. (19), $H^{(II)}$ in Eq. (20), $H^{(III)}$ in Eq. (21), and $H^{(IV)}$ in Eq. (22) of the main text. Note that in order to support n th-order boundary states in a lattice model, the spatial dimension must be $d \geq n$.

Class	Symmetry			$d - n + 1 \pmod{8}$							
	\mathcal{T}	\mathcal{C}	\mathcal{S}	0	1	2	3	4	5	6	7
A	0	0	0	Z^n	0	Z^n	0	Z^n	0	Z^n	0
AIII	0	0	1	0	Z^n	0	Z^n	0	Z^n	0	Z^n
AI	+	0	0	Z^n $H^{(I)}$	0	0	0	$2Z^n$ $H^{(III)}$	0	$Z^{n-1} \times Z_2$	$Z^{n-1} \times Z_2$
BDI	+	+	1	$Z^{n-1} \times Z_2$	Z^n $H^{(II)}$	0	0	0	$2Z^n$ $H^{(IV)}$	0	$Z^{n-1} \times Z_2$
D	0	+	0	$Z^{n-1} \times Z_2$	$Z^{n-1} \times Z_2$	Z^n $H^{(I)}$	0	0	0	$2Z^n$ $H^{(III)}$	0
DIII	-	+	1	0	$Z^{n-1} \times Z_2$	$Z^{n-1} \times Z_2$	Z^n $H^{(II)}$	0	0	0	$2Z^n$ $H^{(IV)}$
AII	-	0	0	$2Z^n$ $H^{(III)}$	0	$Z^{n-1} \times Z_2$	$Z^{n-1} \times Z_2$	Z^n $H^{(I)}$	0	0	0
CII	-	-	1	0	$2Z^n$ $H^{(IV)}$	0	$Z^{n-1} \times Z_2$	$Z^{n-1} \times Z_2$	Z^n $H^{(II)}$	0	0
C	0	-	0	0	0	$2Z^n$ $H^{(III)}$	0	$Z^{n-1} \times Z_2$	$Z^{n-1} \times Z_2$	Z^n $H^{(I)}$	0
CI	+	-	1	0	0	0	$2Z^n$ $H^{(IV)}$	0	$Z^{n-1} \times Z_2$	$Z^{n-1} \times Z_2$	Z^n $H^{(II)}$

$$\tilde{h}_2(k_2, \theta),$$

$$\begin{aligned} \tilde{M}_2(k_2, \theta) &= M_2(k_2) + \lambda_2(1 - \cos \theta), \\ \tilde{h}_2(k_2, \theta) &= \sin(k_2) \cos(2\theta) + 2 \sin(2\theta), \\ \tilde{f}_1(k_2, \theta) &= \sin(2k_2) + \sin(\theta). \end{aligned} \quad (\text{B2})$$

This Hamiltonian preserves the same symmetries as $H_2^{(D,1)}(k_2)$, the original Hamiltonian in Eq. (34), and satisfies $\tilde{H}_2^{(D,1)}(k_2, 0) = H_2^{(D,1)}(k_2)$. Under this interpolation, \tilde{v}_2 does not change for the parameters used in Figs. 4(a) and (b), as shown in Fig. B1(a). But for the trivial cases described in Figs. 4(c) and (d), the topological invariant becomes $\tilde{v}_2 = 2$, as shown in Fig. B1(b). This example demonstrates that the \tilde{v}_2 may change for different interpolations, but the obtained Z_2 topological invariant $v_2 = \tilde{v}_2 \pmod{2}$ for $H_2^{(D,1)}(k_2)$ is unchanged.

Appendix C: First-order topological phases induced by the non-Clifford terms

In this section we will discuss the phases with 1st-order boundary states induced by the non-Clifford terms. More specifically, the longitude non-clifford term can induce a Weyl semimetallic [56, 57] and a weak topological phases [58–60], while the mixed non-Clifford terms only induce the first one.

We first consider cases with the longitude non-Clifford term, $g_1 \sigma_0 \tau_x$. Fig. C1(a) displays its phase diagram in a larger parameter space of g_1 . By increasing g_1 , different pairs of Weyl points will emerge and annihilate along the solid lines in the Figure at different crystal

momenta. Specifically, a pair of Weyl points appears at $(\pi, 0, 0)$ when g_1 reaches the lower black solid line, and annihilates at $(0, 0, 0)$ when g_1 reaches the higher black solid line. Another two pairs of Weyl points appear at $(0, \pi, 0)$ and $(0, 0, \pi)$ for the lower light-blue line, and annihilate at $(\pi, \pi, 0)$ and $(\pi, 0, \pi)$ for the higher light-blue solid line. Finally, the lower (higher) red solid line indicate one pair of Weyl points appear (annihilate) at $(0, \pi, \pi)$ [(π, π, π)]. Combining these information, we obtained several Weyl semimetallic phases, as indicated by claret color in the phase diagram. In addition, two weak topological phases holding gapped bulk and zero-energy 1st-order surface states are seen to emerge between these gapless phases.

To investigate their topological properties, we display the energy spectrum for different parameter in Figs. C1(b) and (e), where we set OBC along r_3 -direction and PBC along other two directions. As expected and discussed in the main text, HOTPs with small g_1 do not hold topologically protected 1st-order boundary states, as shown in Fig. C1(b) for parameters at the red dot in panel (a). Fig. C1(c) and (d) illustrate spectra of the semimetallic phases corresponding to the blue square and yellow triangle in panel (a) respectively, hosting a pair of Weyl points at $(k_1^\pm, 0, 0)$ with $k_1^\pm = \pm \arccos(\frac{(m_1+1)^2 + m_2^2 + 1 - g_1^2}{2(m_1+1)})$. Zero-energy 1st-order boundary states are also seen connect the two Weyl points. Finally, further increasing g_1 have the pair of Weyl points annihilating at $(0, 0, 0)$, driving the system into the weak topological phase with zero-energy 1st-order boundary states for every k_1 [58–60], as displayed in Fig. C1(e).

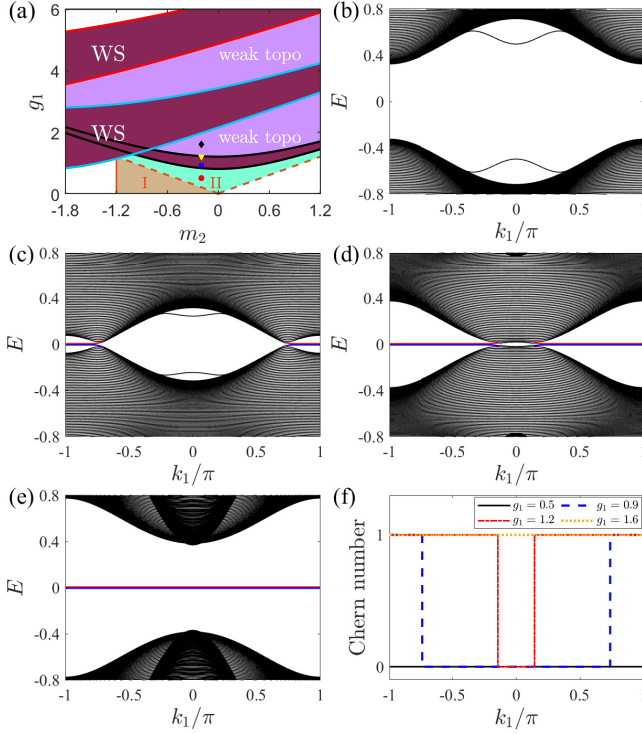


Figure C1. (color online). (a) The phase diagram for Hamiltonian $H^{(D)}(\mathbf{k})$ with the longitudinal non-clifford term $g_1\sigma_0\tau_x$ of Eq. (40) and $m_1 = -1.2$. "WS" and "weak topo" represent the Weyl semimetallic and weak topological phases. (b) to (e) Energy spectra under the OBC along r_3 -direction and PBC along other two directions, where the blue and red lines indicate the surface states. Parameters are (b) $g_1 = 0.5$, (c) 0.9 , (d) 1.2 , (e) 1.6 , corresponding to red dot, blue square, yellow triangle and black diamond in (a), respectively. Other parameters $m_2 = -0.2$ and $k_2 = 0$ for all these panels. Blue and red lines indicate the surface states in (001) and $(00\bar{1})$ surfaces, respectively. (f) The Chern number calculated in k_2 - k_3 space as a function of k_1 for different cases described in (b) to (e).

For both of these two 1st-order topological phases, the topological properties can be described by a Chern number, with the original 3D system taken as pieces of 2D systems of $k_{2,3}$, and $k_1 \in (-\pi, \pi]$ taken as a parameter. In Fig. C1(f), we display the Chern number of the two occupied bands (with negative eigenenergies) as a function of k_1 . We can see that the Chern number is zero for every k_1 for the HOTP, representing a trivial 1st-order topology of this phase. In contrast, the Chern number is nonzero for $k_1 \in (-\pi, k_1^-) \cup (k_1^+, \pi)$ and zero for $k_1 \in (k_1^-, k_1^+)$ for the Weyl semimetallic phase, associated with the values of k_1 with zero-energy 1st-order boundary states in Fig. C1(c) and (d). After the Weyl points annihilate at $(0, 0, 0)$, the Chern number becomes

nonzero for every k_1 , corresponding to the zero-energy 1st-order boundary states shown in Fig. C1(e). We also note that due to the C_4 rotation symmetry in the k_2 - k_3 plane, the results are identical when r_2 -direction takes OBC and other two directions take PBC.

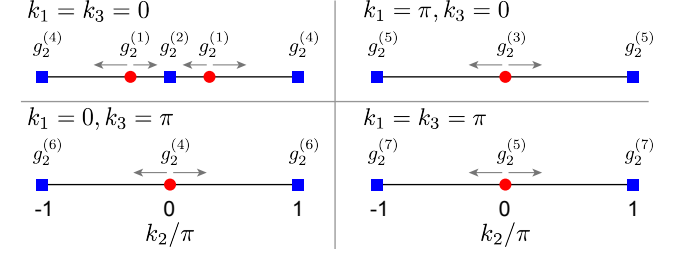


Figure C2. (color online). The creation, annihilation and evolution of Weyl points along high-symmetric lines in the BZ, for the Hamiltonian $H^{(D)}(\mathbf{k})$ with a non-Clifford term $-g_2\sigma_x\tau_z$ (i.e. Eq. (42) in the main text). Red dots (blue squares) indicate the creation (annihilation) of Weyl points at $g_2 = g_2^{(i)}$, as given in Eq. (C1). Gray arrows show the moving directions of Weyl points when increasing g_2 . Here $m_+ = -1.2$ and $m_- = 0.2$ are set.

For the case with a mixed non-Clifford term $-g_2\sigma_x\tau_z$, increasing g_2 is found to induce only semimetallic phases, as shown in the phase diagram in Fig. 8(a) in the main text. Specifically, multiple pairs of Weyl points emerge and annihilate at different crystal momenta with different values of $g_2 = g_2^{(i)}$, with $i = 1, 2, \dots, 7$ and

$$\begin{aligned} g_2^{(1)} &= \sqrt{[2 - (m_+ + 2)^2 + m_-^2]/2}, \\ g_2^{(2)} &= \sqrt{(m_+^2 + m_-^2)/2}, \\ g_2^{(3)} &= \sqrt{[(m_+ + 2)^2 + (m_- + 2)^2]/2}, \\ g_2^{(4)} &= \sqrt{[(m_+ + 4)^2 + m_-^2]/2}, \\ g_2^{(5)} &= \sqrt{[(m_+ + 6)^2 + (m_- + 2)^2]/2}, \\ g_2^{(6)} &= \sqrt{[(m_+ + 8)^2 + m_-^2]/2}, \\ g_2^{(7)} &= \sqrt{[(m_+ + 10)^2 + (m_- + 2)^2]/2}. \end{aligned}$$

The lower black, higher black, and light blue solid lines in Fig. 8(a) are given by $g_2 = g_2^{(1)}$, $g_2^{(2)}$, and $g_2^{(3)}$ respectively. These Weyl points are found to exist only along four high-symmetric lines with $k_{1,3} = 0$ or π , and their emergence, annihilation, and moving direction with increasing g_2 are shown in Fig. C2. To conclude, at least one pair of Weyl points exist for $g_2 \in (g_2^{(1)}, g_2^{(7)})$, and all Weyl points annihilate and disappear when $g_2 > g_2^{(7)}$, resulting in a gapped phase without nontrivial topology.

-
- [1] M. Z. Hasan and C. L. Kane, “Colloquium: Topological insulators,” *Rev. Mod. Phys.* **82**, 3045–3067 (2010).
- [2] X.-L. Qi and S.-C. Zhang, “Topological insulators and superconductors,” *Rev. Mod. Phys.* **83**, 1057–1110 (2011).
- [3] W. A. Benalcazar, B. Andrei Bernevig, and Taylor L. Hughes, “Quantized electric multipole insulators,” *Science* **357**, 61–66 (2017).
- [4] W. A. Benalcazar, B. A. Bernevig, and T. L. Hughes, “Electric multipole moments, topological multipole moment pumping, and chiral hinge states in crystalline insulators,” *Phys. Rev. B* **96**, 245115 (2017).
- [5] Y. Langbehn, J. and Peng, L. Trifunovic, F. von Oppen, and P. W. Brouwer, “Reflection-symmetric second-order topological insulators and superconductors,” *Phys. Rev. Lett.* **119**, 246401 (2017).
- [6] Z. Song, Z. Fang, and C. Fang, “ $(d - 2)$ -dimensional edge states of rotation symmetry protected topological states,” *Phys. Rev. Lett.* **119**, 246402 (2017).
- [7] M. Geier, L. Trifunovic, M. Hoskam, and P. W. Brouwer, “Second-order topological insulators and superconductors with an order-two crystalline symmetry,” *Phys. Rev. B* **97**, 205135 (2018).
- [8] L. Trifunovic and P. W. Brouwer, “Higher-order bulk-boundary correspondence for topological crystalline phases,” *Phys. Rev. X* **9**, 011012 (2019).
- [9] Motohiko Ezawa, “Edge-corner correspondence: Boundary-obstructed topological phases with chiral symmetry,” *Phys. Rev. B* **102**, 121405 (2020).
- [10] Koichi Asaga and Takahiro Fukui, “Boundary-obstructed topological phases of a massive dirac fermion in a magnetic field,” *Phys. Rev. B* **102**, 155102 (2020).
- [11] Xianxin Wu, Wladimir A. Benalcazar, Yinxian Li, Ronny Thomale, Chao-Xing Liu, and Jiangping Hu, “Boundary-obstructed topological high- t_c superconductivity in iron pnictides,” *Phys. Rev. X* **10**, 041014 (2020).
- [12] Apoorv Tiwari, Ammar Jahin, and Yuxuan Wang, “Chiral dirac superconductors: Second-order and boundary-obstructed topology,” *Phys. Rev. Research* **2**, 043300 (2020).
- [13] Eslam Khalaf, Wladimir A. Benalcazar, Taylor L. Hughes, and Raquel Queiroz, “Boundary-obstructed topological phases,” *Phys. Rev. Research* **3**, 013239 (2021).
- [14] M. Ezawa, “Higher-order topological insulators and semimetals on the breathing kagome and pyrochlore lattices,” *Phys. Rev. Lett.* **120**, 026801 (2018).
- [15] F. K. Kunst, G. van Miert, and E. J. Bergholtz, “Lattice models with exactly solvable topological hinge and corner states,” *Phys. Rev. B* **97**, 241405 (2018).
- [16] B.-Y. Xie, H.-F. Wang, H.-X. Wang, X.-Y. Zhu, J.-H. Jiang, M.-H. Lu, and Y.-F. Chen, “Second-order photonic topological insulator with corner states,” *Phys. Rev. B* **98**, 205147 (2018).
- [17] L. Li, M. Umer, and J. Gong, “Direct prediction of corner state configurations from edge winding numbers in two- and three-dimensional chiral-symmetric lattice systems,” *Phys. Rev. B* **98**, 205422 (2018).
- [18] Marc Serra-Garcia, Roman Süssstrunk, and Sebastian D. Huber, “Observation of quadrupole transitions and edge mode topology in an lc circuit network,” *Phys. Rev. B* **99**, 020304 (2019).
- [19] M. Serra-Garcia, V. Peri, R. Süssstrunk, O. R. Bilal, T. Larsen, L. G. Villanueva, and S. D. Huber, “Observation of a phononic quadrupole topological insulator,” *Nature (London)* **555**, 342 (2018).
- [20] F. Schindler, Z. Wang, M. G. Vergniory, A. M. Cook, A. Murani, S. Sengupta, A. Y. Kasumov, R. Deblock, S. Jeon, I. Drozdov, H. Bouchiat, S. Guéron, A. Yazdani, B. A. Bernevig, and T. Neupert, “Higher-order topology in bismuth,” *Nat. Phys.* **15**, 918 (2018).
- [21] C. W. Peterson, W. A. Benalcazar, T. L. Hughes, and G. Bahl, “A quantized microwave quadrupole insulator with topologically protected corner states,” *Nature (London)* **555**, 346 (2018).
- [22] T. Liu, Y.-R. Zhang, Q. Ai, Z. Gong, K. Kawabata, M. Ueda, and F. Nori, “Second-order topological phases in non-hermitian systems,” *Phys. Rev. Lett.* **122**, 076801 (2019).
- [23] C. H. Lee, L. Li, and J. Gong, “Hybrid higher-order skin-topological modes in nonreciprocal systems,” *Phys. Rev. Lett.* **123**, 016805 (2019).
- [24] Y. Peng and G. Refael, “Floquet second-order topological insulators from nonsymorphic space-time symmetries,” *Phys. Rev. Lett.* **123**, 016806 (2019).
- [25] C. Zeng, T. D. Stanescu, C. Zhang, V. W. Scarola, and S. Tewari, “Majorana corner modes with solitons in an attractive hubbard-hofstadter model of cold atom optical lattices,” *Phys. Rev. Lett.* **123**, 060402 (2019).
- [26] X.-W. Luo and C. Zhang, “Higher-order topological corner states induced by gain and loss,” *Phys. Rev. Lett.* **123**, 073601 (2019).
- [27] R.-X. Zhang, W. S. Cole, X. Wu, and S. Das Sarma, “Higher-order topology and nodal topological superconductivity in fe(se,te) heterostructures,” *Phys. Rev. Lett.* **123**, 167001 (2019).
- [28] Z. Wang, B. J. Wieder, J. Li, B. Yan, and B. A. Bernevig, “Higher-order topology, monopole nodal lines, and the origin of large fermi arcs in transition metal dichalcogenides xte_2 ($x = \text{Mo}, \text{W}$),” *Phys. Rev. Lett.* **123**, 186401 (2019).
- [29] X.-L. Sheng, C. Chen, H. Liu, Z. Chen, Z.-M. Yu, Y. X. Zhao, and S. A. Yang, “Two-dimensional second-order topological insulator in graphdiyne,” *Phys. Rev. Lett.* **123**, 256402 (2019).
- [30] C.-A. Li, B. Fu, Z.-A. Hu, J. Li, and S.-Q. Shen, “Topological phase transitions in disordered electric quadrupole insulators,” *Phys. Rev. Lett.* **125**, 166801 (2020).
- [31] Dumitru Călugăru, Vladimir Juričić, and Bitan Roy, “Higher-order topological phases: A general principle of construction,” *Phys. Rev. B* **99**, 041301 (2019).
- [32] Yao Wang, Yongguan Ke, Yi-Jun Chang, Yong-Heng Lu, Jun Gao, Chaohong Lee, and Xian-Min Jin, “Constructing higher-order topological states in higher dimensions,” *Phys. Rev. B* **104**, 224303 (2021).
- [33] W. A. Benalcazar and A. Cerjan, “Chiral-symmetric higher-order topological phases of matter,” *Phys. Rev. Lett.* **128**, 127601 (2022).
- [34] L. Li, W. Zhu, and J. Gong, “Direct dynamical characterization of higher-order topological phases with nested band inversion surfaces,” *Sci. Bull.* **66**, 1502–1510 (2021).
- [35] M. R. Zirnbauer, “Riemannian symmetric superspaces and their origin in random-matrix theory,” *J. Math.*

- Phys. (N.Y.) **37**, 4986–5018 (1996).
- [36] A. Altland and M. R. Zirnbauer, “Nonstandard symmetry classes in mesoscopic normal-superconducting hybrid structures,” *Phys. Rev. B* **55**, 1142–1161 (1997).
 - [37] S. Ryu, A. P. Schnyder, A. Furusaki, and A. W. W. Ludwig, “Topological insulators and superconductors: tenfold way and dimensional hierarchy,” *New J. Phys.* **12**, 065010 (2010).
 - [38] C.-K. Chiu, J. C. Y. Teo, A. P. Schnyder, and S. Ryu, “Classification of topological quantum matter with symmetries,” *Rev. Mod. Phys.* **88**, 035005 (2016).
 - [39] A Yu Kitaev, “Unpaired majorana fermions in quantum wires,” *Phys. Usp.* **44**, 131–136 (2001).
 - [40] S. R. Elliott and M. Franz, “Colloquium: Majorana fermions in nuclear, particle, and solid-state physics,” *Rev. Mod. Phys.* **87**, 137–163 (2015).
 - [41] L. Zhang, L. Zhang, S. Niu, and X.-J. Liu, “Dynamical classification of topological quantum phases,” *Sci. Bull.* **63**, 1385–1391 (2018).
 - [42] X.-L. Yu, W. Ji, L. Zhang, Y. Wang, J. Wu, and X.-J. Liu, “Quantum dynamical characterization and simulation of topological phases with high-order band inversion surfaces,” *PRX Quantum* **2**, 020320 (2021).
 - [43] Linhu Li and Jiangbin Gong, “Probing higher-order band topology via spin texture measurements: quantum simulation,” *Science Bulletin* **66**, 1817–1818 (2021).
 - [44] R. S. K. Mong and V. Shivamoggi, “Edge states and the bulk-boundary correspondence in dirac hamiltonians,” *Phys. Rev. B* **83**, 125109 (2011).
 - [45] L. Li, H. H. Yap, M. A. N. Araújo, and J. Gong, “Engineering topological phases with a three-dimensional nodal-loop semimetal,” *Phys. Rev. B* **96**, 235424 (2017).
 - [46] A chiral symmetry seem to emerge for $H_2^{(I)}(\mathbf{k}_{1,\parallel})$ due to the absence of $\Gamma_{(2p+1)}^{1,2}$, yet the Hilbert space of this effective Hamiltonian can be reduced to 2^{p-1} dimension, where the chiral symmetry is ruled out.
 - [47] Linhu Li and Miguel A. N. Araújo, “Topological insulating phases from two-dimensional nodal loop semimetals,” *Phys. Rev. B* **94**, 165117 (2016).
 - [48] X.-L. Qi, T. L. Hughes, and S.-C. Zhang, “Topological field theory of time-reversal invariant insulators,” *Phys. Rev. B* **78**, 195424 (2008).
 - [49] L. Li, C. Yang, and S. Chen, “Topological invariants for phase transition points of one-dimensional z2 topological systems,” *Eur. Phys. J. B* **89**, 195 (2016).
 - [50] D. Xiao, M.-C. Chang, and Q. Niu, “Berry phase effects on electronic properties,” *Rev. Mod. Phys.* **82**, 1959–2007 (2010).
 - [51] L. Zhang, W. Jia, and X.-J. Liu, “Universal topological quench dynamics: Altland-zirnbauer tenfold classes,” *arXiv* **2104**, 00617 (2021).
 - [52] Mahmoud Lababidi, Indubala I. Satija, and Erhai Zhao, “Counter-propagating edge modes and topological phases of a kicked quantum hall system,” *Phys. Rev. Lett.* **112**, 026805 (2014).
 - [53] Y. Yoshimura, K.-I. Imura, T. Fukui, and Y. Hatsugai, “Characterizing weak topological properties: Berry phase point of view,” *Phys. Rev. B* **90**, 155443 (2014).
 - [54] Muhammad Umer, Raditya Weda Bomantera, and Jiangbin Gong, “Counterpropagating edge states in floquet topological insulating phases,” *Phys. Rev. B* **101**, 235438 (2020).
 - [55] The minus sign means that g_2 functions as $-g_3$ after the rotation. This is associated with the minus sign in defining $\tilde{\Gamma}_2$.
 - [56] N. P. Armitage, E. J. Mele, and A. Vishwanath, “Weyl and dirac semimetals in three-dimensional solids,” *Rev. Mod. Phys.* **90**, 015001 (2018).
 - [57] B. Q. Lv, T. Qian, and H. Ding, “Experimental perspective on three-dimensional topological semimetals,” *Rev. Mod. Phys.* **93**, 025002 (2021).
 - [58] L. Fu, C. L. Kane, and E. J. Mele, “Topological insulators in three dimensions,” *Phys. Rev. Lett.* **98**, 106803 (2007).
 - [59] J. E. Moore and L. Balents, “Topological invariants of time-reversal-invariant band structures,” *Phys. Rev. B* **75**, 121306 (2007).
 - [60] R. Roy, “Topological phases and the quantum spin hall effect in three dimensions,” *Phys. Rev. B* **79**, 195322 (2009).
 - [61] Wenchao Ma, Longwen Zhou, Qi Zhang, Min Li, Chunyang Cheng, Jianpei Geng, Xing Rong, Fazhan Shi, Jiangbin Gong, and Jiangfeng Du, “Experimental observation of a generalized thouless pump with a single spin,” *Phys. Rev. Lett.* **120**, 120501 (2018).
 - [62] Xinsheng Tan, YX Zhao, Qiang Liu, Guangming Xue, Hai-Feng Yu, ZD Wang, and Yang Yu, “Simulation and manipulation of tunable weyl-semimetal bands using superconducting quantum circuits,” *Physical review letters* **122**, 010501 (2019).
 - [63] Wentao Ji, Lin Zhang, Mengqi Wang, Long Zhang, Yuhang Guo, Zihua Chai, Xing Rong, Fazhan Shi, Xiong-Jun Liu, Ya Wang, *et al.*, “Quantum simulation for three-dimensional chiral topological insulator,” *Physical Review Letters* **125**, 020504 (2020).
 - [64] Tao Xin, Yishan Li, Yu-ang Fan, Xuanran Zhu, Yingjie Zhang, Xinfang Nie, Jun Li, Qihang Liu, and Dawei Lu, “Quantum phases of three-dimensional chiral topological insulators on a spin quantum simulator,” *Physical Review Letters* **125**, 090502 (2020).
 - [65] Pedram Roushan, C Neill, Yu Chen, M Kolodrubetz, C Quintana, N Leung, M Fang, R Barends, B Campbell, Z Chen, *et al.*, “Observation of topological transitions in interacting quantum circuits,” *Nature* **515**, 241–244 (2014).
 - [66] L. Zhang, L. Zhang, and X.-J. Liu, “Dynamical detection of topological charges,” *Phys. Rev. A* **99**, 053606 (2019).
 - [67] L. Zhang, L. Zhang, and X.-J. Liu, “Characterizing topological phases by quantum quenches: A general theory,” *Phys. Rev. A* **100**, 063624 (2019).
 - [68] L. Zhang, L. Zhang, and X.-J. L., “Unified theory to characterize floquet topological phases by quench dynamics,” *Phys. Rev. Lett.* **125**, 183001 (2020).
 - [69] Yue-Hui Lu, Bao-Zong Wang, and Xiong-Jun Liu, “Ideal weyl semimetal with 3d spin-orbit coupled ultracold quantum gas,” *Science Bulletin* **65**, 2080–2085 (2020).
 - [70] L. Zhang, L. Zhang, and X.-J. Liu, “Quench-induced dynamical topology under dynamical noise,” *Phys. Rev. Research* **3**, 013229 (2021).
 - [71] Jingjing Niu, Tongxing Yan, Yuxuan Zhou, Ziyu Tao, Xiaole Li, Weiyang Liu, Libo Zhang, Hao Jia, Song Liu, Zhongbo Yan, *et al.*, “Simulation of higher-order topological phases and related topological phase transitions in a superconducting qubit,” *Science Bulletin* **66**, 1168–1175 (2021).
 - [72] Chang-Rui Yi, Long Zhang, Lin Zhang, Rui-Heng Jiao, Xiang-Can Cheng, Zong-Yao Wang, Xiao-Tian Xu, Wei

- Sun, Xiong-Jun Liu, Shuai Chen, *et al.*, “Observing topological charges and dynamical bulk-surface correspondence with ultracold atoms,” *Physical review letters* **123**, 190603 (2019).
- [73] Z.-Y. Wang, X.-C. Cheng, B.-Z. Wang, J.-Y. Zhang, Y.-H. Lu, C.-R. Yi, S. Niu, Y. Deng, X.-J. Liu, S. Chen, and J.-W. Pan, “Realization of an ideal weyl semimetal band in a quantum gas with 3d spin-orbit coupling,” *Science* **372**, 271–276 (2021).
- [74] M. Lin and T. L. Hughes, “Topological quadrupolar semimetals,” *Phys. Rev. B* **98**, 241103 (2018).
- [75] B. J. Wieder, Z. Wang, J. Cano, X. Dai, L. M. Schoop, B. Bradlyn, and B. A. Bernevig, “Strong and fragile topological dirac semimetals with higher-order fermi arcs,” *Nat. Commun.* **11**, 627 (2020).
- [76] W. Wu, Z.-M. Yu, X. Zhou, Y. X. Zhao, and S. A. Yang, “Higher-order dirac fermions in three dimensions,” *Phys. Rev. B* **101**, 205134 (2020).
- [77] B. Roy, “Higher-order topological superconductors in \mathcal{P} -, \mathcal{T} -odd quadrupolar dirac materials,” *Phys. Rev. B* **101**, 220506 (2020).
- [78] H.-X. Wang, Z.-K. Lin, B. Jiang, G.-Y. Guo, and J.-H. Jiang, “Higher-order weyl semimetals,” *Phys. Rev. Lett.* **125**, 146401 (2020).
- [79] R. Chen, T. Liu, C. M. Wang, H.-Z. Lu, and X. C. Xie, “Field-tunable one-sided higher-order topological hinge states in dirac semimetals,” *Phys. Rev. Lett.* **127**, 066801 (2021).